Electromagnetic Induction Systems for Discrimination among Metallic Targets

Except where reference is made to the work of others, the work described in this dissertation is my own or was done in collaboration with my advisory committee. This dissertation does not include proprietary or classified information.

Venkata Sailaja Chilaka

Certificate of Approval:

Jitendra K. Tugnait Professor Electrical and Computer Engineering	Lloyd S. Riggs, Chair Professor Electrical and Computer Engineering
Stuart M. Wentworth Associate Professor Electrical and Computer Engineering	Michael E. Baginski Associate Professor Electrical and Computer Engineering
Prathima Agrawal Professor Electrical and Computer Engineering	Stephen L. McFarland Dean Graduate School

Electromagnetic Induction Systems for Discrimination among Metallic Targets

Venkata Sailaja Chilaka

A Dissertation

Submitted to

the Graduate Faculty of

Auburn University

in Partial Fulfillment of the

Requirements for the

Degree of

Doctor of Philosophy

Auburn, Alabama
May 11, 2006

Electromagnetic Induction Systems for Discrimination among Metallic Targets

Venkata Sailaja Chilaka

_____

Signature of Author

_____

Date of Graduation

Dissertation Abstract

Electromagnetic Induction Systems for Discrimination among Metallic Targets

Venkata Sailaja Chilaka

Doctor of Philosophy, May 11, 2006
(M.S.E.E., The University of Texas at Dallas, 2001)
(B.Tech., Jawaharlal Nehru Technological University - Hyderabad, India, 1998)

94 Typed Pages

Directed by Lloyd S. Riggs

This dissertation discusses the ability of time- and frequency-domain electromagnetic induction (EMI) systems to discriminate unexploded ordnance (UXO) from clutter. The chief contribution of this work is to demonstrate the importance of extremely low frequency (ELF) data in discrimination of thick and thin-walled ferrous UXO-like targets that are otherwise visually identical. It is demonstrated that when data in the 30 Hz to 24 kHz range is extended down to 1 Hz discrimination performance improves by a factor of 1.5. Improved discrimination performance reduces false alarms and ultimately lowers remediation costs.

Acknowledgments

First and foremost the author would like to thank Dr. Lloyd Riggs for his inspiration and extensive guidance. For his friendship and invaluable help she will forever be grateful. Special thanks to Daniel Faircloth for his FEM model which gave a better insight into the research problem. She would like to extend her thanks to Dr. Jitendra Tugnait for his valuable suggestions on statistical part of the research, and to Dr. Stuart Wentworth and Dr. Michael Baginski for providing constructive comments on her dissertation. She thanks her research team for the wonderful work environment and funfilled lunch hours.

She is grateful to Dr. Prathima Agrawal and Vodafone-US foundation for supporting her through fellowship, and Strategic Environmental Research and Development (SERDP) for funding the research.

To all her friends, the author is thankful for their constant support. She expresses her gratitude to her parents for their prayers, for putting her on the right path, and teaching her to dream big and chase it. She thanks her parents-in-law for their immense understanding. She is indebted to her husband Ravi for his love, sacrifice, patience and persistent encouragement. Last but most important she is thankful to Almighty God who gives her the best always.

Style manual or journal used IEEE Transactions on Geoscience and Remote Sensing(together with the style known as "auphd").

Computer software used The document preparation package TeXnicCenter and LaTeXwith the style-file `auphd.sty`.

Table of Contents

List of Figures

List of Tables

Chapter 1

Introduction

Unexploded ordnance (UXO) are devastating weapons (bombs, mortars, shells, grenades, etc.) that did not explode when they were employed [1]. These remnants of ongoing conflicts, past wars (as far back as the First World War) and military training have contaminated vast areas all over the world. UXO pose a threat to the environment and lives of innocent civilians, thus leaving millions of acres of land uninhabitable. It is not a problem being faced by third world countries alone, it is one of the most pervasive environmental problems faced by the U.S. Department of Defense (DOD). In the United States, 6 million acres of land is contaminated with UXO, most of which is a result of past and present military ranges or training sites [2]. Due to their high metallic content, UXO are much easier to detect than to discriminate. It is estimated that 70% of UXO remediation costs are going toward the investigation of false positives (non-UXO items and "dry holes"). Clearly effective discrimination between UXO and clutter is necessary to reduce remediation costs [3].

The discrimination problem has captured the attention of many researchers in the past decade and the detection technologies currently being used or proposed for this purpose include acoustic sensors, biological odor sensors (dogs and bees), electromagnetic induction (EMI), ground penetrating radar (GPR), infrared (IR), magnetometry, synthetic aperture radar (SAR), trace gas analysis and combinations of these technologies [3] - [9]. Moreover, research and development efforts are underway

in exploring new technologies and in combining current technologies [6]. Table 1.1 summarizes strengths and limitations of four different detection/discrimination technologies. The performance of each of these technologies depends on different factors such as the dimensions and constitution of the UXO, the depth at and medium in which it is buried. Prominent among all ordnance detection technologies are magnetometers and EMI sensors, as they are fairly simple, cheap and reasonably well understood. A magnetometer is a passive sensor which uses the earth's magnetic field as excitation source to measure an object's magnetic susceptibility. On the other hand an EMI sensor is an active device that carries an excitation source and measures magnetic susceptibility and electrical conductivity depending on the frequency of excitation [10].

The Multi-sensor Towed Array Detection System (MTADS) developed by Naval Research Laboratory, comprising of magnetometers and EMI sensors achieved a detection rate of 95% [11]. However, it still suffers a high false-alarm rate, thus presenting a need for a more efficient and cost-effective discrimination system. The work presented in this dissertation is part of a project funded by the Strategic Environmental Research and Development Program (SERDP) to develop an ordnance-specific EMI sensor that combines detection with discrimination [12].

Table 1.1: Strengths and limitations of UXO detection technologies [3] - [9]

Technology	**Strengths**	**Limitations**
Acoustics	• Immune to metallic clutter • Good for plastic mine detection • Best suited to underwater detection	• Inability to detect deep targets • Limited discrimination between high metallic targets like UXO
Electromagnetic Induction	• Relatively immune to geologic noise • Ability to determine target shape, size and orientation	• False alarms due to metal fragments • Sensitive to sensor orientation • Inability to determine target depth
Magnetometry	• Easy to use • Ability to detect deep targets	• Prone to geologic noise • Inability to determine target shape
Ground Penetrating radar	• Ability to determine target depth and shape • Reduces false alarm when used with other sensor technologies	• Reduced efficiency in wet and/or clay rich soils • Not proven to be a standalone UXO sensor

Many researchers have proved that electromagnetic induction (EMI) has potential for classification and identification [13] - [32]. Based on the operating mode, EMI sensors can be classified as time domain (TD) (pulsed induction, PI) systems or frequency domain (FD) (continuous wave, CW) systems. A time domain system operates by employing short pulses of current with rapid turn-off time and the target information lies in the decay characteristics of the received signal [15] - [22]. The simplest time domain EMI sensor is a metal detector and it has been in use for subsurface target detection for many decades [33] . On the other hand, a frequency domain system operates at a single or discrete set of frequencies and the received signal (spectrum) provides target information [23] - [32]. The basic concept of Electromagnetic Induction Spectroscopy (EMIS) for the purpose of subsurface target identification has been introduced by Won et al [33]. It is a well-known fact that the time- and frequency-domain responses form a Fourier transform pair [34], [16] and therefore, both responses should contain the same information. However, due to practical constraints, it is difficult to acquire certain information using one system or the other. Therefore, the relative limitations of each system will affect their respective discrimination capabilities.

The goal of this research is to study the discrimination capabilities of both time- and frequency-domain EMI systems and in particular, to evaluate the importance of extremely low frequency CW EMI response in improving the discrimination of visually identical UXO-like targets of different wall thicknesses.

Wait derived the EMI response of a conducting sphere [34] in a uniformly time-varying magnetic field. Grant and West [35] showed that this response can be expressed as a product of a coupling term and response function, where the coupling

term depends on geometry and orientation of the object, and the response function depends on frequency and the object's material properties. In order to study the effect of wall thickness on the response of visually identical targets, the work of Grant and West has been extended to a conducting and permeable spherical shell and its analytical response is derived. In Chapter 2, the theoretical response of a conducting loop, and solid and hollow spheres are presented in order to acquaint the reader with the general response characteristics of conducting and/or permeable targets.

The response of the spherical shell indicates that extremely low frequency magnetic fields in the range of 1 to 30Hz can be used to penetrate deep into ferrous targets and thereby reveal their subsurface characteristics. The subsurface information can in turn be used to improve discrimination performance over what can be achieved using a commercial system with a typical EMI spectrum extending from ∼30Hz up to ∼24kHz. Similarly, differences in the time-domain EMI response of visually identical objects due to difference in wall thickness are not observable until many milliseconds after the transmitter current turn off. Therefore, to improve discrimination over what is currently available with commercially available EMI instruments, there is a need for a CW system with its bandwidth extended to extremely low frequencies or equivalently a pulsed system with its time capture range extended to late-time. Time- and frequency-domain EMI systems with respective extended ranges were built and a careful study of different practical difficulties and trade-offs involved in their design are described in Chapter 3.

The prototype CW and pulsed systems are used to measure the response of various targets including loops, spheres, thin- and thick-walled cylinders and inert UXOs. The measurements are validated using a numerical model (finite element

method) as illustrated in Chapter 4. It was observed that the responses of thin and thick walled cylinders were practically indistinguishable above 30Hz (the low frequency limit of the popular Geophex GEM-3 sensor). However, variations among the responses were easily discernible if the operating frequency was extended down to 1Hz due to the significant skin depth at those frequencies. Likewise, numerical simulations show that similar information might be available from a time-domain system if very late-time data is captured. However, discrimination based on the late-time data is hindered by low signal-to-noise ratio. Therefore, efforts are currently underway to construct a time-domain EMI sensor with improved sensitivity and noise characterization at late-times (more than 10ms after the transmitter current turn off).

The key contribution of this work is to provide a statistically based quantitative measure of the improvement in discrimination performance obtained by extending the EMI frequency response downward to 1Hz relative to what can be achieved using the typical EMI spectrum that extends from ∼30Hz upward to ∼24kHz. Specifically, in Chapter 5 three statistical tests are developed to discriminate between UXO-like targets. Applying this inference-based statistical test shows that at a probability of false alarm of 20%, probability of correct identification is only 60% using the restricted bandwidth whereas using the extended frequency range the probability of correct identification improves to 90% at the same false alarm rate.

Although extending the typical EMI spectrum to extremely low frequencies substantially improves discrimination performance, a price must be paid for the additional information acquired. A single point collected at 1Hz takes 1 second but often many data records must be averaged to achieve adequate signal-to-noise ratio so in general it is very time-consuming indeed to collect a sufficient number of data points

in the 1Hz to 30Hz frequency range to adequately represent a target's (especially a ferrous target's) low frequency spectrum. A slow data acquisition rate causes the EMI data acquisition to be sensitive to motion and therefore, when acquiring very low frequency data, it is necessary for the system to remain stationary with respect to the target. This and other practical implementation issues are discussed in Chapter 6 along with suggestions for possibly fruitful future research.

Chapter 2

Electromagnetic Induction Theory

2.1 Introduction

In this chapter the reader is first introduced to the basic concept of electromagnetic induction theory. Next, time and frequency responses of a conducting loop are derived using a simple circuit analysis of the EMI system and significant features of the response are explained. After that, EMI response of a solid sphere is derived as a boundary-value problem to show that the features presented in simple loop response are still valid for a three-dimensional object. By examining the response of the solid sphere one can observe the effect of permeability on the object's response. The response of a hollow sphere is derived to study the effect of wall thickness on an object's response. The general form of the response of an arbitrarily shaped object is also presented.

2.2 Circuit Representation of EMI system

According to Faraday's law, time-varying electric current through a transmitter coil radiates a primary magnetic field. This field may in turn induce eddy currents in any nearby conductive and/or permeable object. The eddy currents in turn radiate a secondary magnetic field which is sensed using a receiver coil. The received signal may be used to acquire information regarding the target and ultimately used

for detection and discrimination purposes. When source frequencies are low or the transmitter currents do not change too rapidly the above electromagnetic interaction may be referred to as electromagnetic induction (EMI) thus emphasizing magnetic (or quasi-magnetostatic) processes. Typical components of an EMI system are shown in Figure 2.1 and include a transmitter and receiver coil and buried object or objects.

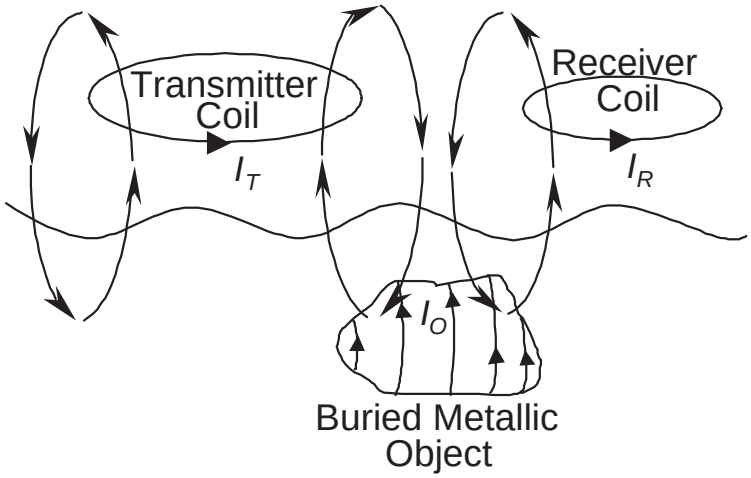

Figure 2.1: Typical EMI system

Figure 2.2 represents the equivalent frequency- and time-domain circuit models of the EMI system shown in Figure 2.1. In Figures 2.2(a) and 2.2(b) the transmitter, receiver and object are represented by their equivalent resistance and inductance pairs (R, L) [35] . The subscripts T, R and O represent transmitter, receiver and object respectively. Note that this circuit representation of an object is exact only for a simple first order target like a q-coil (thin copper loop) and does not hold for complex objects like spheres and cylinders. Further, I_T, I_R and I_O correspond to the transmitter, receiver, and object currents. Note that I_T is a sinusoidal signal in CW EMI but would manifest as a short duration pulse of current in pulsed EMI

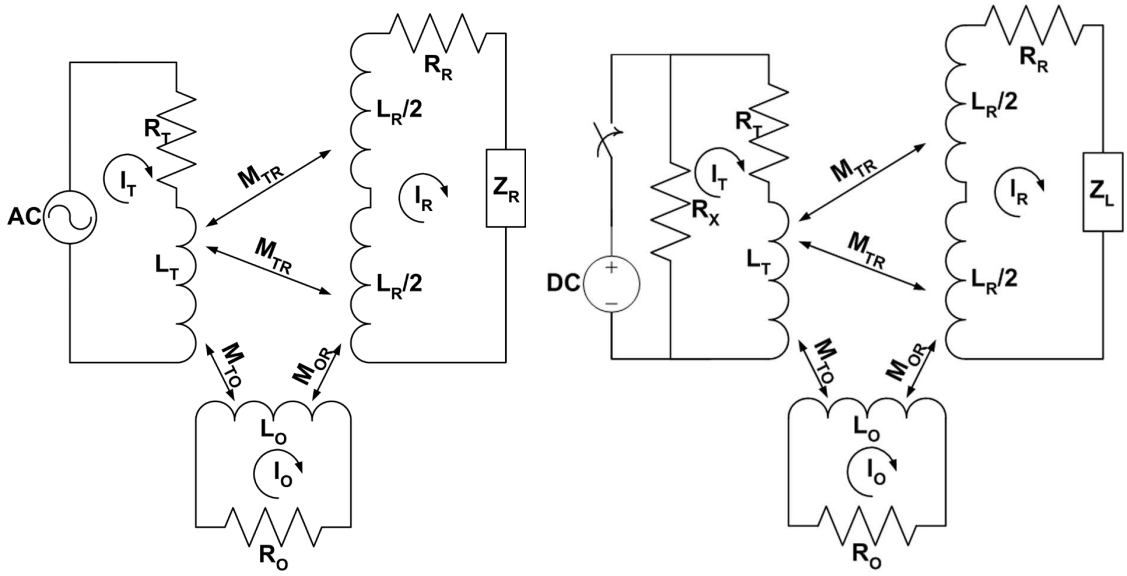

Figure 2.2: Circuit Model of (a) CW EMI system (b) pulsed EMI system

systems. The mutual coupling between transmitter and object, object and receiver, and transmitter and receiver is M_{TO}, M_{OR} and M_{TR} respectively. Because of magnetic coupling between the transmitter and object (M_{TO}) a current I_O is induced in the buried object. Similarly, coupling between the object and receiver coil, M_{OR}, results in a voltage V_{OBJECT}. Finally, because of direct coupling between the transmitter and receiver coils, M_{TR}, a direct (as opposed to object coupled) voltage exists at the receiver, termed V_{DIRECT}. The direct coupled voltage is usually undesirable and efforts are often made to reduce its magnitude with respect to that of the object coupled voltage (i.e. it is best to have $V_{DIRECT} << V_{OBJECT}$). By superposition, the net voltage at the receiver is V_{OUT}= V_{OBJECT}+ V_{DIRECT}. It is desirable to reduce V_{DIRECT} such that the output voltage is almost equal to the voltage due only to the object. This can be achieved by using a figure-8 receiver coil, also known as a bucking coil. This configuration consists of two N turn coils of opposite polarity, connected in

series such that equal flux passing through them will produce an equal and opposite voltage in each coil. The net voltage is therefore theoretically zero in the absence of an object. The figure-8 receiver coil is represented in the circuit diagram by splitting the receiver coil inductance each half with inductance $L_R/2$.

In the case of a pulsed system it is desirable to turn off the transmitter current as rapidly as possible without oscillations because the induced voltage in the object is proportional to the derivative of the transmitter current. A shunt resistance R_X may be used to dampen oscillations due to second order interaction between the parasitic capacitance and the transmitter coil inductance. The resistance R_X insures a rapid and smooth turn-off of the transmitter current. Similarly, R_Y reduces the oscillations in the receiver coil. Further, Z_R and Z_L are the input impedances of the receiver coil amplifiers for the CW and pulsed systems respectively.

The EMI responses of a loop and a conducting sphere have been derived by several authors including Wait [34], and Grant and West [35]. These will be presented here in the same order to provide the reader with an understanding of the response function for relatively simple objects.

2.3 EMI Response of a Conducting Loop

First, assuming that Z_R is infinity (open circuit), and applying Kirchoff's Voltage Law to the circuit in Figure 2.2(a) yields

$$I_O(R_O + j\omega L_O) + j\omega M_{TO} I_T = 0 \tag{2.1}$$

$$V_{OBJECT} = j\omega M_{OR} I_O \tag{2.2}$$

$$V_{DIRECT} = j\omega M_{TR} I_T \tag{2.3}$$

Simple manipulation of these three equations results in

$$\frac{V_{OBJECT}}{V_{DIRECT}} = \left(\frac{-M_{TO}M_{OR}}{L_O M_{TR}}\right)\left(\frac{\alpha^2 + j\alpha}{1+\alpha^2}\right) \tag{2.4}$$

where $\alpha = \omega/\omega_O = \omega L_O/R_O$ is the response parameter, ω is the radian frequency and ω_O is the radian break frequency. V_{OBJECT}/V_{DIRECT} represents the response of the EMI system to an object where $\left(\frac{-M_{TO}M_{OR}}{L_O M_{TR}}\right)$ is the coupling coefficient and $\left(\frac{\alpha^2+j\alpha}{1+\alpha^2}\right)$ is the response function. As $M_{ij} = k_{ij}\sqrt{L_i L_j}$, the coupling coefficient reduces to $\left(\frac{k_{TO}k_{OR}}{k_{TR}}\right)$ and equation (2.4) is now given by

$$\frac{V_{OBJECT}}{V_{DIRECT}} = \underbrace{\left(\frac{-k_{TO}k_{OR}}{k_{TR}}\right)}_{\substack{\text{Coupling}\\ \text{Coefficient}}}\underbrace{\left(\frac{\alpha^2 + j\alpha}{1+\alpha^2}\right)}_{\substack{\text{Response}\\ \text{Function}}} \tag{2.5}$$

In equation (2.5), only the response function depends on the frequency of the current and electrical properties of the loop, and the coupling coefficient depends on the physical size and location of the loop with respect to the transmitter and receiver coils. The real and imaginary parts of the response function are shown in Figure 2.3(a) and magnitude and phase are shown in 2.3(b). As $\alpha \to 0$ the real part of response function shown in Figure 2.3(a) tends to zero faster than the imaginary part resulting in a purely imaginary response for small α which is given by

$$\lim_{\alpha\to 0}\frac{V_{OBJECT}}{V_{DIRECT}} = -\frac{j\omega L}{R}\frac{k_{TO}k_{OR}}{k_{TR}}. \tag{2.6}$$

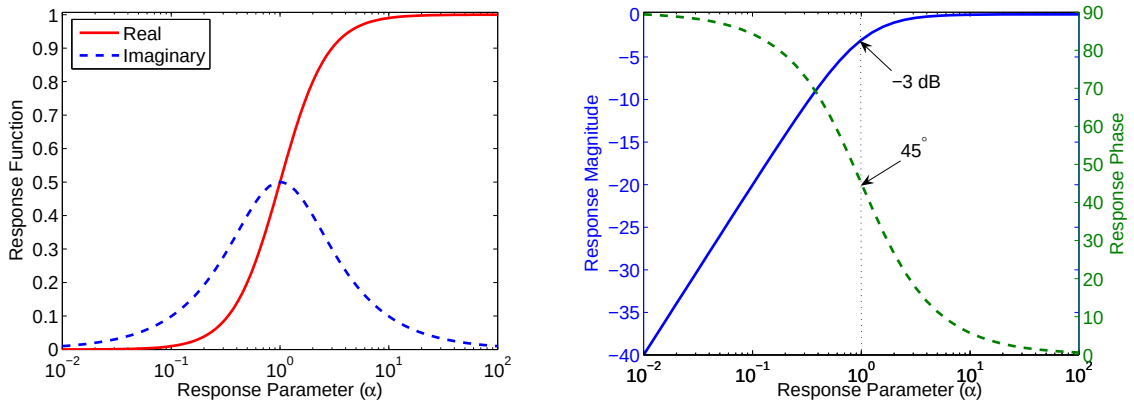

(a) (b)

Figure 2.3: Frequency response of a thin copper loop (simple first order target)

and is referred to as the resistive limit. Similarly, as $\alpha \to \infty$, the imaginary part of the response function vanishes, and the real part asymptotically approaches unity. Under this condition the response is given by

$$\lim_{\alpha \to 0} \frac{V_{OBJECT}}{V_{DIRECT}} = -\frac{k_{TO} k_{OR}}{k_{TR}} \tag{2.7}$$

which is referred to as the inductive limit. The crossover frequency in Figure 2.3(a) or equivalently 45° frequency in Figure 2.3(b) is where the real and imaginary parts of the response function are equal. The quadrature peak as the name suggests is where the imaginary response is maximum. Observe from Figure 2.3(b) that the thin copper loop acts like a high pass filter with a break (3dB) frequency at $\alpha = 1$ or $f_{\text{break}} = R_O/(2\pi L_O)$. In this particular case, crossover frequency and quadrature peak coincide with the break frequency, which may not be true for three dimensional permeable targets as shown in subsequent sections.

Now, if a finite Z_R is assumed, finite currents flow in the receiver circuit. If we also assume that receiver coil currents are much less than currents in the transmitter

coil, then only the transmitter current will induce a voltage in the object. This assumption results in

$$\frac{V_{OBJECT}}{V_{DIRECT}} = \frac{-k_{TO}k_{OR}}{k_{TR}} \left(\frac{\alpha^2 + j\alpha}{1+\alpha^2} \right) \frac{Z_R}{Z_R + Z_{COIL}} \tag{2.8}$$

where $Z_{COIL} = R_R + j\omega L_R$. If Z_R is a simple resistor, the object response is modified by the low-pass filter function $(1 + j\omega/\omega_B)^{-1}$ where $\omega_B = R/L_R$ is the radian break frequency of the low-pass filter. This means R should be large enough such that ω_B is much greater than the highest frequency of interest. However, R cannot be too high as this will force current to flow through the parasitic capacitance of the receiver coil. Therefore, it is desirable for the parasitic capacitance to be as small as possible so that R can be increased. This, in turn, will result in an increased measurement bandwidth.

As stated earlier, time and frequency domain responses form a Fourier transform pair, and therefore the time domain response can be derived by taking an inverse Fourier transform (IFT) of the frequency domain response. However, for a loop, it is straightforward to solve the circuit model directly in time domain and which also provides better insight into the problem.

Kirchhoff's voltage law applied to the object loop yields

$$\left[R_O + L_O \frac{d}{dt} \right] I_O(t) = -M_{TO} \frac{dI_T(t)}{dt} \tag{2.9}$$

where $I_T(t)$ is given by

$$I_T(t) = \begin{cases} I_I & t < 0 \\ I_I\left(1 - \frac{t}{T}\right) & 0 \leq t < T \\ 0 & t > T \end{cases} \tag{2.10}$$

where I_I is the initial current. Substituting equation (2.10) in equation (2.9) and solving for $I_O(t)$ gives

$$I_O(t) = \begin{cases} 0 & t < 0 \\ \frac{M_{TO}I_I}{R_O T}\left(1 - e^{-t/\tau}\right) & 0 \leq t < T \\ \frac{M_{TO}I_I}{R_O T}\left(1 - e^{-T/\tau}\right)e^{-(t-T)/\tau} & t > T \end{cases} \tag{2.11}$$

where $\tau = L_O/R_O$ is the time constant of the exponential decay. Note that the object eddy currents and receiver voltage are inversely proportional to the turn-off time of the transmitter current and thus, assuming a constant noise level, detection/discrimination improves as the turn-off time of the transmitter current decreases. Therefore, the turn-off time should be much smaller than the object time constant ($T << \tau$), in order to achieve good signal-to-noise ratio. If $t < T$ then $t << \tau$. Substituting the small value approximation into a Taylor series expansion for the exponential functions ($e^x = 1 + x$ for small x) in equation (2.11) yields

$$I_O(t) = \begin{cases} 0 & t < 0 \\ \frac{M_{TO}I_I}{L_O T}t & 0 \leq t < T \\ \frac{M_{TO}I_I}{L_O}e^{-t/\tau} & t > T \end{cases} \tag{2.12}$$

Furthermore, the voltage at the receiver due to direct coupling with the transmitter current (equation (2.10)) is

$$V_{DIRECT} = -M_{TR}\frac{d}{dt}I_T(t) = \begin{cases} 0 & t < 0 \\ \frac{M_{TR}I_I}{T} & 0 \le t \le T \\ 0 & t > T \end{cases} \tag{2.13}$$

Similarly, the voltage at the receiver due to the object current (equation (2.12)) is

$$V_{OBJECT} = -M_{OR}\frac{d}{dt}I_O(t) = \begin{cases} 0 & t < 0 \\ \frac{-M_{OR}M_{TO}I_I}{L_O T} & 0 \le t \le T \\ \frac{M_{OR}M_{TO}I_I}{L_O \tau}e^{-t/\tau} & t > T \end{cases} \tag{2.14}$$

The resulting total receiver output voltage is $V_{OUT} = V_{OBJECT} + V_{DIRECT}$.

$$V_{OUT} = \begin{cases} 0 & t < 0 \\ \frac{M_{TR}I_I}{T} - \frac{M_{OR}M_{TO}I_I}{L_O T} & 0 \le t < T \\ \frac{M_{OR}M_{TO}I_I}{L_O \tau}e^{-t/\tau} & t > T \end{cases} \tag{2.15}$$

Figure 2.4 shows the normalized current and voltage waveforms of a TD system. V_{OUT} is not given in since it is simply the sum of the object voltage and the direct voltage. For $t < T$, V_{OUT} may vary depending on the magnitude of both object and direct voltages. However, V_{OUT} for $t > T$ is of primary interest, and it is ideally due only to the object eddy currents.

It is worthwhile to mention the relationship between time and frequency domain responses. For a simple first order target like a thin copper loop, the time constant

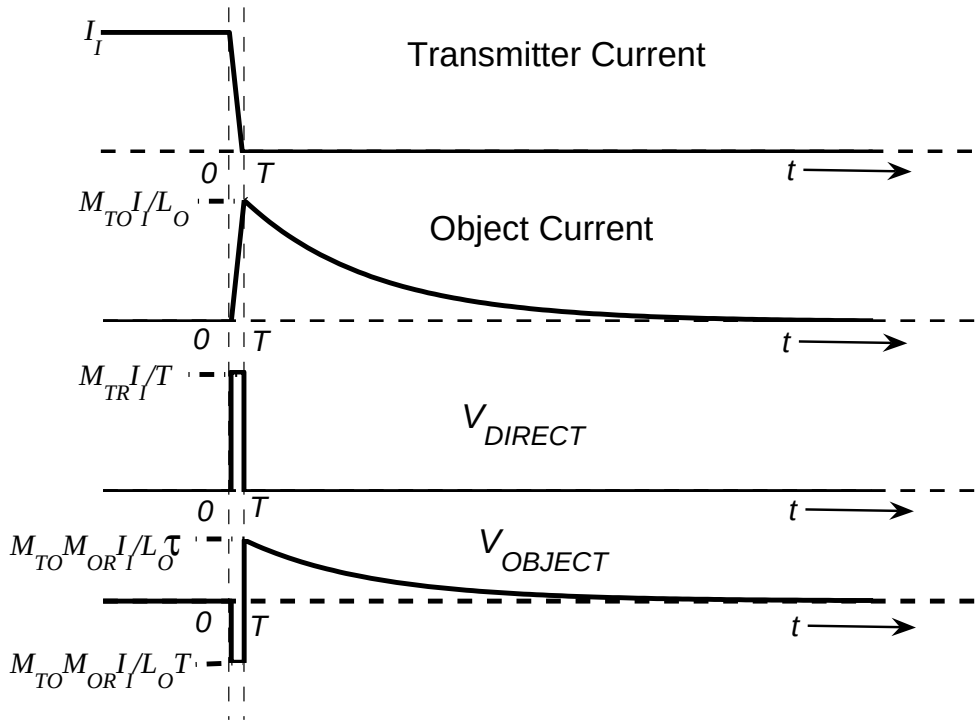

Figure 2.4: Current and voltage waveforms at different stages of the pulsed EMI system

($\tau = L_O/R_O$) of the exponential decay is the inverse of the radian break frequency or crossover frequency ($\omega_O = R_O/L_O$) of the frequency response. For complex objects like the ferrous sphere or cylinder, the time domain response is not a simple exponential decay and in the frequency response, the quadrature peak and crossover frequencies do not coincide with the break frequency. However, the response of a ferrous sphere is in the form of a power-law in early time followed by an exponential decay that reflects the residual signal due to the lowest mode eddy currents [23]. Moreover, the transition from power-law to exponential decay corresponds approximately to the quadrature peak in the frequency response [23].

2.4 EMI Response of a Conducting Sphere [35]

A simple circuit model representation of $(R_O + j\omega L_O)$ is not valid for objects like the sphere and cylinder. Therefore, in this section a boundary value problem is solved to derive the response of a conducting and permeable sphere in a uniform, time-varying magnetic field [35, 36]. Figure 2.5 shows a sphere with its center located

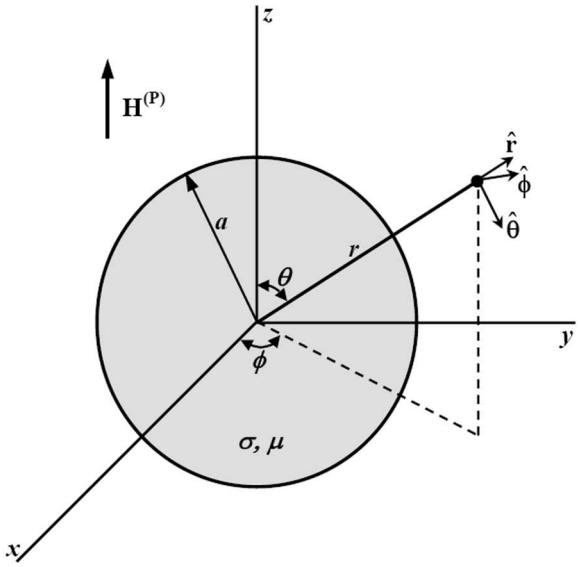

Figure 2.5: Conducting sphere in a uniform magnetic field

at the origin of a spherical coordinate system and the primary field in the direction of the polar axis. With these assumptions the primary field can be expressed as

$$\mathbf{H^{(P)}} = H\cos\theta\hat{\mathbf{r}} - H\sin\theta\hat{\boldsymbol{\theta}} = \boldsymbol{\nabla}\times\frac{1}{2}Hr\sin\theta\hat{\boldsymbol{\phi}} \tag{2.16}$$

and $\mathbf{H^{(P)}} = \boldsymbol{\nabla}\times\mathbf{A^{(P)}}$, which means that the primary field $\mathbf{H^{(P)}}$ can be obtained from a vector potential

$$\mathbf{A^{(P)}} = \frac{1}{2}Hr\sin\theta\hat{\boldsymbol{\phi}} \tag{2.17}$$

The vector potential must satisfy the diffusion equations

$$\nabla^2 \mathbf{A} - j\omega\sigma\mu\mathbf{A} = 0 \qquad \boldsymbol{\nabla} \cdot \mathbf{A} = 0 \tag{2.18}$$

where $\mathbf{A} = A(r,\theta)\hat{\boldsymbol{\phi}} = -A(r,\theta)\sin\phi\hat{\mathbf{x}} + A(r,\theta)\cos\phi\hat{\mathbf{y}}$.

Operating the Laplacian operator separately on each of the rectangular components of $\mathbf{A}$ and recombining them gives

$$\nabla^2 \mathbf{A} = \left(\nabla^2 A - \frac{A}{r^2\sin^2\theta}\right)\hat{\boldsymbol{\phi}} \tag{2.19}$$

which is a linear scalar equation that can be solved by the method of separation of variables, where it is assumed that there exists a solution such that

$$A(r,\theta) = R(r)\Theta(\theta) \tag{2.20}$$

Substituting equation (2.20) into equation (2.19), results in two ordinary differential equations - a modified Bessel equation and an associated Legendre equation, which are expressed as

$$(1-u^2)\frac{d^2\Theta}{du^2} - 2u\frac{d\Theta}{du} - \left[\frac{1}{(1-u^2)} - n(n+1)\right]\Theta = 0 \tag{2.21}$$

and

$$\frac{d^2R}{dr^2} + \frac{2}{r}\frac{dR}{dr} - \left[k^2 + \frac{n(n+1)}{r^2}\right]R = 0 \tag{2.22}$$

where $u = \cos\theta$, $k^2 = j\omega\sigma\mu$ and n is the separation constant. Equation (2.21) has a solution of the form P_n^1, and Equation (2.22) has two possible solutions $r^{-1/2}I_{n+1/2}(kr)$

and $r^{-1/2}I_{-n-1/2}(kr)$ when $k \neq 0$, and when $k = 0$ (i.e., $\sigma = 0$), equation (2.22) reduces to

$$\frac{d}{dr}\left(r^2\frac{dR}{dr}\right) - n(n+1)R = 0 \tag{2.23}$$

which has the solution

$$R(r) = Cr^n + Dr^{-(n+1)} \tag{2.24}$$

Since $P_1^1(u) = \sin\theta$, the vector potential in equation (2.17) can be written as

$$\mathbf{A}^{(\mathbf{P})} = \frac{1}{2}HrP_1^1(u)\hat{\boldsymbol{\phi}} \tag{2.25}$$

where P_1^1 is the Legendre polynomial with separation constant $n = 1$. The general solutions of equation (2.18) can now be written for region 1 (outside sphere) and region 2 (inside sphere). In region 1, the field must be the sum of a primary field (equation (2.25)) and an induction field (with $n = 1$) that vanishes at infinity. Therefore, the vector potential in region 1 is given as

$$A_1 = A^{(P)} + A^{(S)} = \frac{1}{2}HrP_1^1(u) + Dr^{-2}P_1^1(u) \tag{2.26}$$

and in region 2, as there can be no singularities, the potential is given as

$$A_2 = FP_1^1(u)r^{-1/2}I_{3/2}(kr) \tag{2.27}$$

The boundary conditions to be applied at the surface of the sphere ($r = a$) are

1. the magnetic field tangential to the interface is continuous

$$\mathbf{n} \times (\mathbf{H_1} - \mathbf{H_2}) = 0 \tag{2.28}$$

2. the magnetic flux density normal to the interface is continuous

$$\mathbf{n}\cdot(\mu_1\mathbf{H_1} - \mu_2\mathbf{H_2}) = 0 \tag{2.29}$$

These two boundary conditions in terms of the vector potential are

$$\begin{aligned} A_1 &= A_2 \\ \frac{1}{\mu_0}\frac{\partial}{\partial r}(rA_1) &= \frac{1}{\mu}\frac{\partial}{\partial r}(rA_2) \end{aligned} \tag{2.30}$$

Substituting equations (2.26) and (2.27) in equation (2.30), and solving for D yields

$$D = -\frac{a^3\mu_0 H}{2}\left[\frac{(\mu_0/2 - 2\mu)I'_{3/2}(ka) + \mu_0 kaI'_{3/2}(ka)}{(\mu_0/2 + \mu)I'_{3/2}(ka) + \mu_0 kaI'_{3/2}(ka)}\right] \tag{2.31}$$

The derivatives of the Bessel functions are

$$I'_n(x) = I_{n-1} - \frac{n}{x}I_n(x) = I_{n+1}(x) + \frac{n}{x}I_n(x) \tag{2.32}$$

which reduce the Bessel functions in equation (2.31) to $I'_{1/2}$ and $I'_{-1/2}$ which are expressed in terms of hyperbolic functions as

$$I_{1/2}(ka) = \sqrt{\frac{2}{\pi ka}}\sinh(ka) \quad \text{and} \quad I_{-1/2}(ka) = \sqrt{\frac{2}{\pi ka}}\cosh(ka) \tag{2.33}$$

Substituting these into equation (2.31) yields

$$D = -\frac{a^3\mu_0 H}{2}\left\{\frac{[\mu_0(1+k^2a^2)+2\mu]\sinh(ka)-(2\mu+\mu_0)ka\cosh(ka)}{[\mu_0(1+k^2a^2)-\mu]\sinh(ka)+(\mu-\mu_0)ka\cosh(ka)}\right\} \tag{2.34}$$

Therefore,

$$\begin{aligned}\mathbf{A}^{(\mathbf{S})} &= Dr^{-2}P_1^1(u)\hat{\boldsymbol{\Phi}} = -\frac{\mu_0\sin\theta}{4\pi r^2}2\pi a^3 H \\ &\times \left\{\frac{[\mu_0(1+k^2a^2)+2\mu]\sinh(ka)-(2\mu+\mu_0)ka\cosh(ka)}{[\mu_0(1+k^2a^2)-\mu]\sinh(ka)+(\mu-\mu_0)ka\cosh(ka)}\right\}\hat{\boldsymbol{\Phi}}\end{aligned} \tag{2.35}$$

If the complex quantity in the braces is represented as $(X + jY)$, then the moment of magnetic dipole oriented in the direction of the polar axis is

$$m = -2\pi a^3 H(X + jY) \tag{2.36}$$

Note that $(X+jY)$ is the only term in equation (2.35) which depends on the frequency of the field and electrical properties of the sphere. So, $(X+jY)$ is the response function of a sphere and is plotted for different values of relative permeability and presented in Figure 2.6. The response function of a nonpermeable sphere is similar to that of a copper loop except that the real part of the response reaches its inductive limit at frequencies higher than that of the loop. For a relative permeability greater than one (e.g. ferrous target), the real part of the response tends to some negative value as the response parameter tends to zero. This DC asymptote becomes increasingly negative with increasing permeability and approaches -2 for $\mu_r \to \infty$. Also, the low-frequency asymptote for permeable sphere is not reached until frequencies well below 30Hz and therefore cannot be captured with 30Hz to 24kHz band commercial

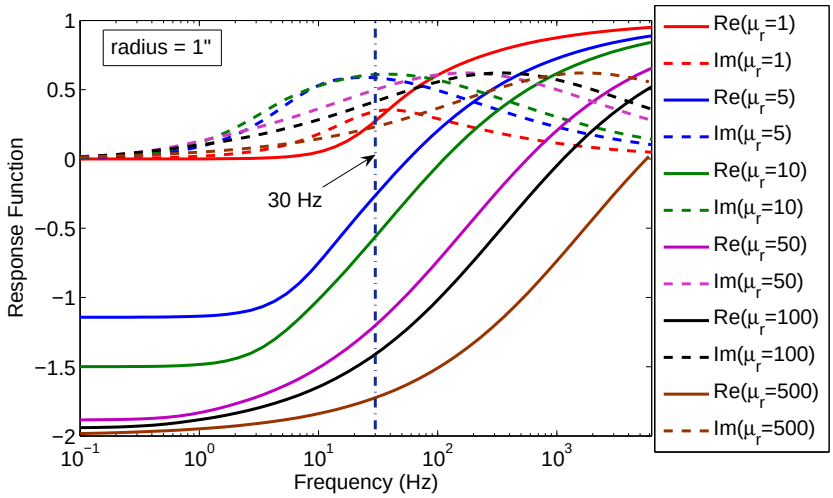

Figure 2.6: Response function of a sphere in uniform magnetic field

systems. Figure 2.7 shows the magnitude and phase responses of spheres. Note from Figures 2.7(a) and 2.7(b) that only the nonpermeable sphere has a high-pass response like a copper loop and all permeable spheres have a predominantly low-pass response. Moreover, the phase response of the nonpermeable sphere starts at 90° and asymptotes to 0° at high frequencies (Figure 2.7(c)), while that of the permeable sphere starts at 180° and asymptotes to 0° at high frequencies (Figure 2.7(d)).

2.5 EMI Response of a Conducting Spherical Shell

As UXOs are hollow objects filled with an explosive, the response of a spherical shell is derived to study the effect of wall-thickness on a target's response. The sphere problem in the previous section is extended to a spherical shell by satisfying boundary-conditions at both the boundaries (between regions 1 and 2, and 2 and 3) as shown in Figure 2.5. For this problem, the vector potential in each region is given

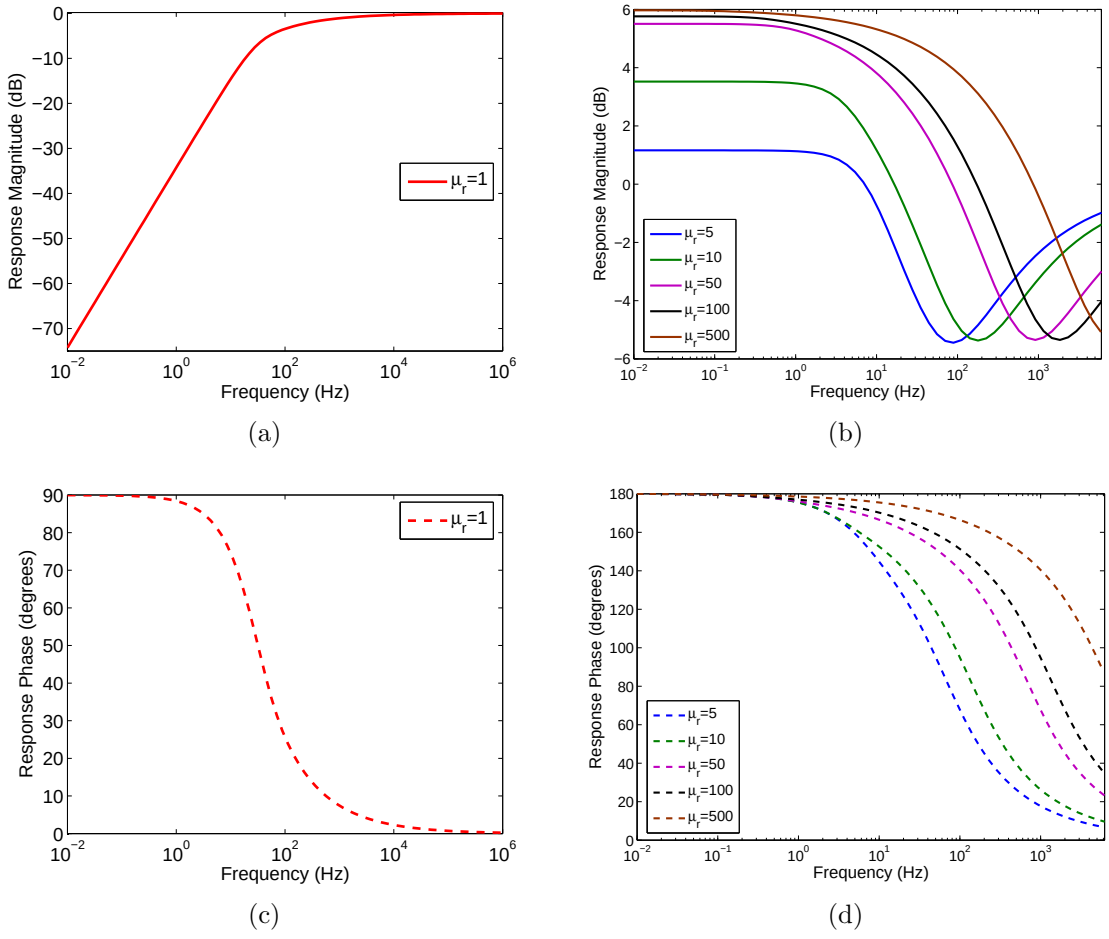

Figure 2.7: (a) Magnitude (b) Phase responses of a sphere

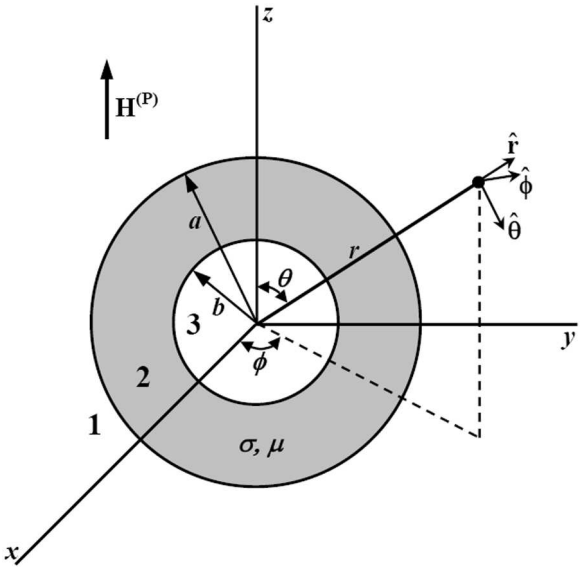

Figure 2.8: Conducting spherical shell in a uniform magnetic field

by

$$\begin{aligned} A_1 &= \left[\frac{1}{2}\mu_0 H_0 r + Dr^{-2}\right] P_1^1(u) \\ A_2 &= \left[FI_{3/2}(kr) + GK_{3/2}(kr)\right] r^{-1/2} P_1^1(u) \\ A_3 &= CrP_1^1(u) \end{aligned} \tag{2.37}$$

Note that A_1 is same as A_1 for the solid sphere because fields should vanish at infinity. A_2 is chosen to avoid singularities and A_3 is chosen such that fields are zero at the origin. The boundary conditions at $r = a$ and $r = b$ are

$$\begin{aligned} A_1 &= A_2|_{r=a} \\ A_2 &= A_3|_{r=b} \\ \frac{1}{\mu_0}\frac{\partial}{\partial r}(rA_1) &= \frac{1}{\mu}\frac{\partial}{\partial r}(rA_2)|_{r=a} \\ \frac{1}{\mu_0}\frac{\partial}{\partial r}(rA_2) &= \frac{1}{\mu}\frac{\partial}{\partial r}(rA_3)|_{r=b} \end{aligned} \tag{2.38}$$

Solving these boundary conditions for D yields

$$D = -\frac{\mu_0 H a^3}{2}\left[\frac{n_{11}n_{12} - n_{21}n_{22}}{d_{11}d_{12} - d_{21}d_{22}}\right] \tag{2.39}$$

where

$$\begin{aligned}
n_{11} &= \left(\frac{\mu_0}{2} - 2\mu\right) I_{3/2}(ka) + \mu_0 ka I'_{3/2}(ka) \\
n_{21} &= \left(\frac{\mu_0}{2} - 2\mu\right) K_{3/2}(ka) + \mu_0 ka K'_{3/2}(ka) \\
d_{11} &= \left(\mu + \frac{\mu_0}{2}\right) I_{3/2}(ka) + \mu_0 ka I'_{3/2}(ka) \\
d_{21} &= \left(\mu + \frac{\mu_0}{2}\right) K_{3/2}(ka) + \mu_0 ka K'_{3/2}(ka) \\
d_{12} = n_{12} &= \left(\frac{\mu_0}{2} - 2\mu\right) K_{3/2}(kb) + \mu_0 kb K'_{3/2}(kb) \\
d_{22} = n_{22} &= \left(\frac{\mu_0}{2} - 2\mu\right) I_{3/2}(kb) + \mu_0 kb I'_{3/2}(kb)
\end{aligned}$$

This equation can be verified by considering $b \to 0$ (i.e., solid sphere) where n_{22} and d_{22} tend to 0

$$\begin{aligned}
D|_{b\to 0} &= \frac{-\mu_0 H a^3}{2}\left[\frac{n_{11}}{d_{11}}\right] \\
&= -\frac{a^3 \mu_0 H}{2}\left[\frac{(\mu_0/2 - 2\mu) I'_{3/2}(ka) + \mu_0 ka I'_{3/2}(ka)}{(\mu_0/2 + \mu) I'_{3/2}(ka) + \mu_0 ka I'_{3/2}(ka)}\right]
\end{aligned} \tag{2.40}$$

which is the same expression as in equation (2.31) for the solid sphere.

The secondary vector potential $\mathbf{A}^{(\mathbf{S})}$ can be derived just as in the sphere problem. The response of a ferrous spherical shell is plotted for different values of inner radius in Figure 2.9. The values for σ and μ_r are chosen to match those of ferrous cylinders that will be addressed in Chapter 4. Observe that above 30Hz it is hard to distinguish

even the thinnest wall shell ($b = 2.75''$) from the solid sphere ($b = 0''$). Clearly at very low frequencies, nominally below 30Hz, the wall thickness can be clearly discerned. Therefore, for large ferrous targets, valuable target information for discrimination purposes exists at very low frequencies.

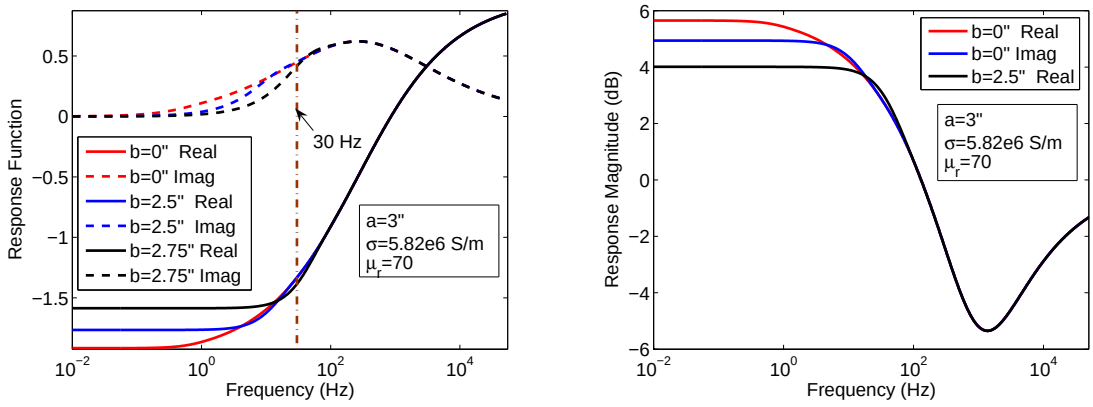

(a) (b)

Figure 2.9: (a) Real and imaginary (b) Magnitude responses of ferrous ($\mu = 70\mu_0$, $\sigma = 5.82 \times 10^6$ S/m) spherical shells with fixed outer radius ($a = 5$ cm) and different inner radii

2.6 EMI Response of an Arbitrary Permeable Conducting Target

The sphere and spherical shell are objects with three-dimensional symmetry and therefore, have analytical models. In contrast, rotationally symmetric objects like finite cylinders do not have a simple closed form analytical solution. Liao and Carin [45] give

$$M(\omega) = diag[m_{p0} + \sum_k \frac{\omega m_{pk}}{\omega - j\omega_{pk}}, m_{p0} + \sum_k \frac{\omega m_{pk}}{\omega - j\omega_{pk}}, m_{z0} + \sum_k \frac{\omega m_{zk}}{\omega - j\omega_{zk}}] \quad (2.41)$$

as the magnetization tensor of a rotationally symmetric object with the z-direction taken as the axis of rotation. (The object's scattered field is proportional to its magnetization tensor.) Observe that each component of the magnetization tensor is composed of an infinite sum of terms of weight m_{zk} and m_{pk} for the component along and perpendicular to the object's axis of rotation, respectively. Unlike the objects treated above, the frequency response of arbitrarily shaped conducting bodies is represented by a superposition of high pass terms, but in many cases only the lowest-order component has significant strength allowing one to replace the summation in $M(\omega)$ with a single term which will be the object's response function. If the excitatory magnetic field is aligned with the axis of the object, then all m_{pk} are zero and vice versa. In general, though, both components will be excited. Also, m_{p0} and m_{zp} give the DC (zero frequency) response and both are zero for nonmagnetic targets.

Although equation (2.41) is valuable for general expository purposes, actual computation for m_{zk}, m_{pk}, ω_{zk}, and ω_{pk} is not at all straightforward. Therefore, numerical methods have to be used to compute the scattered field for body-of-revolution geometries. Several numerical methods previously applied to the UXO problem include Integral Equations (IE) [40], [46]- [52], Method of Moments (MoM) [53]- [56], and Finite Element Method-Boundary Element Method (FEM-BEM) [37]. In order to ensure that the results (presented in chapter 4) obtained using our EMI sensor are correct, the measured responses of steel cylinders are compared with the Finite Element Method (FEM) model developed by Faircloth [57].

2.7 Summary

A typical electromagnetic induction system has a transmitter coil, receiver coil and a buried metallic target, and operates according to Faraday's law. A simple circuit analysis of the EMI system yields transient and frequency responses of a conducting loop where the transient response is exponential and the frequency response is high-pass.

The EMI response of a solid sphere presents the effect of permeability on the object's response. The frequency response is high-pass for a nonpermeable sphere (just like that of the conducting loop) whereas it is low-pass for a permeable sphere.

The response of a hollow sphere was derived and it was shown that the responses of spherical shells with fixed outer radius but different wall thicknesses are identical above 30Hz. However below 30Hz, the responses are distinct because the fields at low frequencies penetrate into the object and reveal its inner structure.

Therefore, frequencies below 30Hz are necessary to acquire the information necessary to discriminate among visually identical objects with varying wall thicknesses.

Chapter 3

EMI Sensor Description

3.1 Introduction

Analytical responses of permeable solid and hollow spheres presented in Chapter 2 show that important target information is contained in the extremely low frequency or equivalently in the late time EMI response. The CW and pulsed EMI systems designed to acquire extended data ranges are explained in this chapter. Also, major design tradeoffs germane to the development of such systems are discussed.

3.2 Experimental setup

The operation of CW and pulsed EMI systems is described utilizing block diagrams and digitized photographs of the corresponding hardware configurations are also presented.

3.2.1 CW System

Figure 3.1 presents a generic block diagram of the CW measurement system. The Hewlett Packard 89410A Vector Signal Analyzer forms the heart of the measurement system and provides stimulus and measures the coherent response of any test target. The analyzer's source is programmed to provide excitation at a discrete number (51, 101, 401, or 801) of uniformly spaced frequencies anywhere within the operating range from near DC to 10 MHz.

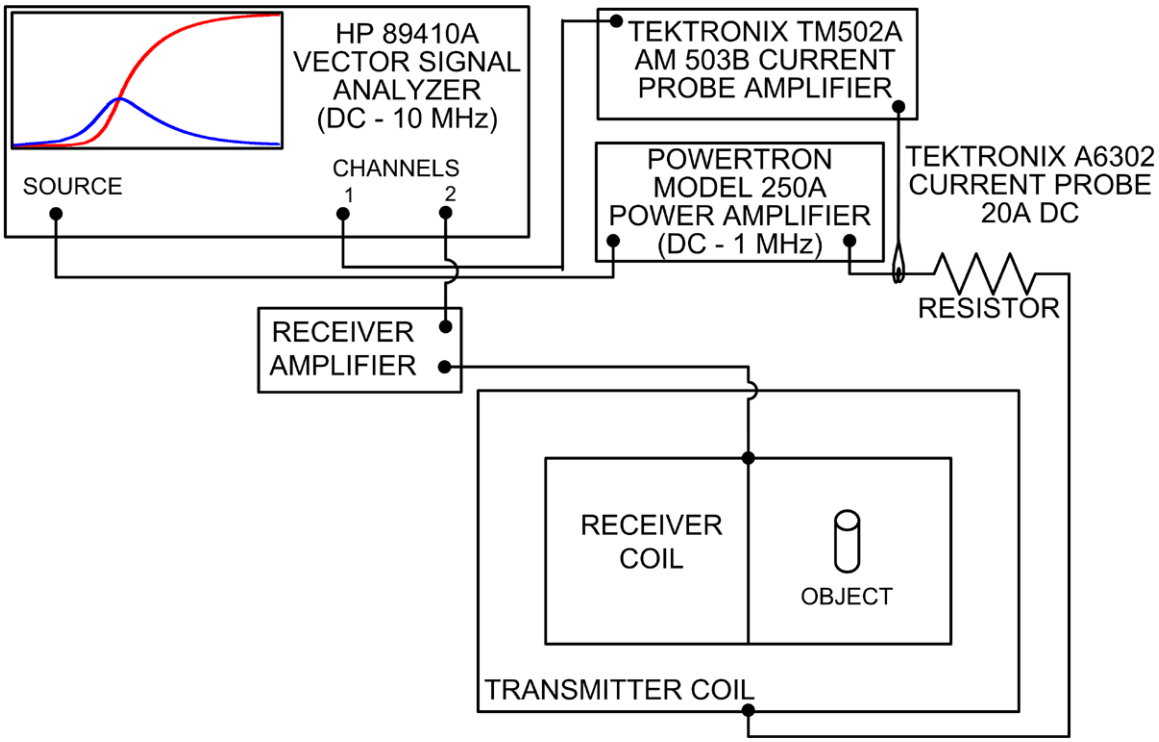

Figure 3.1: Block Diagram of a CW EMI system

The analyzer's source drives a Powertron Model 250A Power Amplifier (250Watts) which boosts the current flowing in the transmitter coil. The current flowing through the transmitter coil is measured using a Tektronix TM502A current probe and fed to channel one of the analyzer. The resistance R is used to limit the transmitter current due to low coil impedance at low frequencies. The receiver coil consisting of N clockwise and N counterclockwise turns should ideally have zero output voltage when symmetrically located with respect to the transmitting coil. Any object that is not symmetrically located with respect to the transmitter coil will induce a voltage at the output of the receiver coil. This voltage, representing the object response, is amplified by the receiver coil amplifier that in turn is connected to channel two of the analyzer. In order to determine the object transfer function the analyzer is programmed to compute the frequency response (ratio of voltage at channel two to

the current at channel one) divided by $j\omega$ over the range of frequencies of interest (refer to equation (2.4)).

Figure 3.2 shows the hardware configuration corresponding to Figure 3.1.

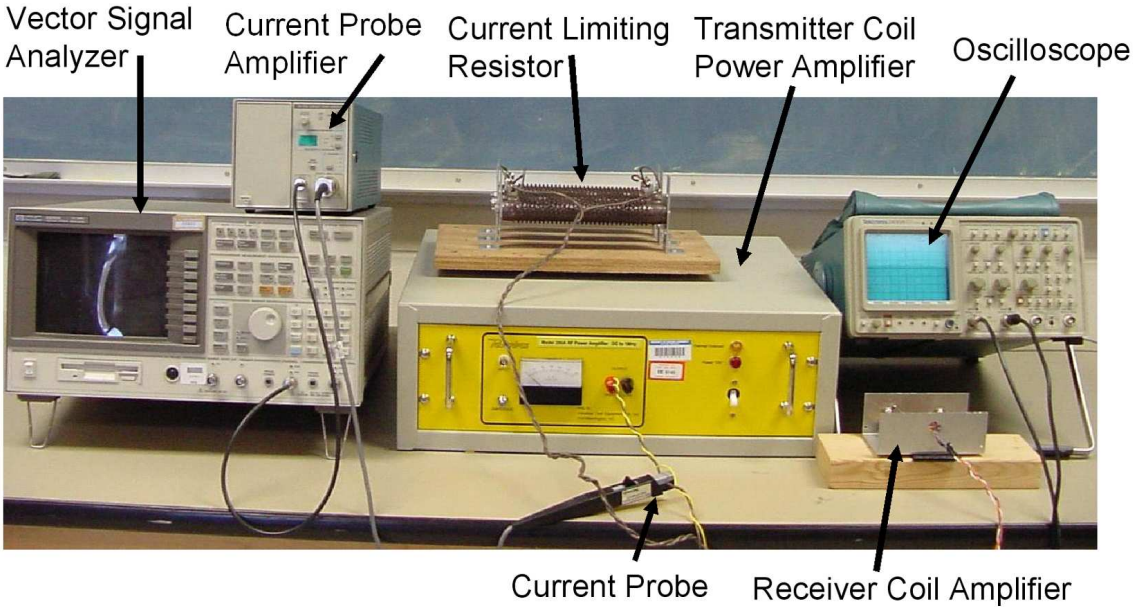

Figure 3.2: Hardware setup of a CW EMI system

3.2.2 Pulsed System

In a pulsed EMI system the four major components are the sensor coils, pulser, signal conditioning unit and data acquisition package as shown in Figure 3.3. The sensor coils are the same as in the CW system and are described in next section. A PIC Microcontroller PIC16F88 is used to generate a pulse waveform, which switches the insulated gate bipolar transistor (IGBT) on and off. When the pulse waveform is "high" the switch closes and allows current I_T to flow through the transmitter coil for the duration of the pulse. When the pulse falls below a characteristic "low" the switch is opened. The pulse duration is chosen to be 800μs, which is sufficient time for the

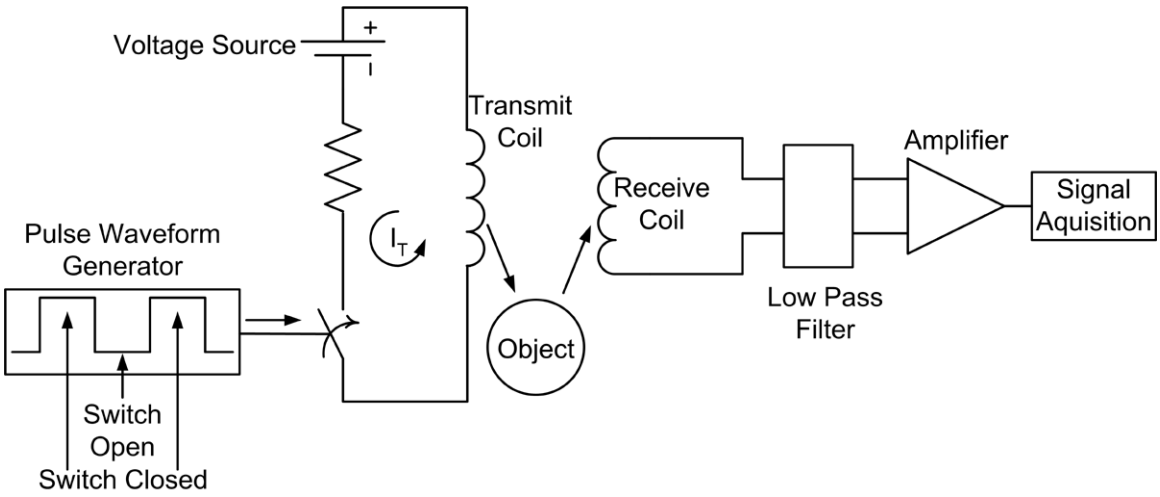

Figure 3.3: Block Diagram of pulsed EMI system

transmitter current to reach a steady maximum value ($\sim$ 18A with 24V power supply). As mentioned in the previous chapter, rapid transmitter current turn-off is necessary for inducing large object currents. Rapid turn-off is insured by driving the IGBT with a MOSFET/IGBT driver chip IXDN404PI from IXYS Corporation. The transmitter current falls to zero in approximately 0.5μs. It is also important that the current pulse remains "off" long enough to permit the receiver coil to capture the object's response which may be of significant amplitude for tens of milliseconds. Hence, the pulse repetition rate is chosen to be 50Hz (20ms period). The object's response captured by the receiver coil is passed through the signal conditioning unit which consists of a current-to-voltage converter, and an amplifier with low-pass filter characteristics (3dB frequency = 10 kHz). The signal conditioning unit converts the receiver coil current into a voltage with more gain, and also filters out high frequency noise. The amplified and filtered analog receiver voltage is then digitized using analog-to-digital (AD) data acquisition card, Compuscope (CS)1602. The Gagescope software is used to display the waveform and record the data. The hardware configuration for the pulsed system

is shown in Figure 3.4. The "pulser box" in Figure 3.5 contains various components including IGBT, MOSFET driver, PIC Microcontroller and receiver amplifier.

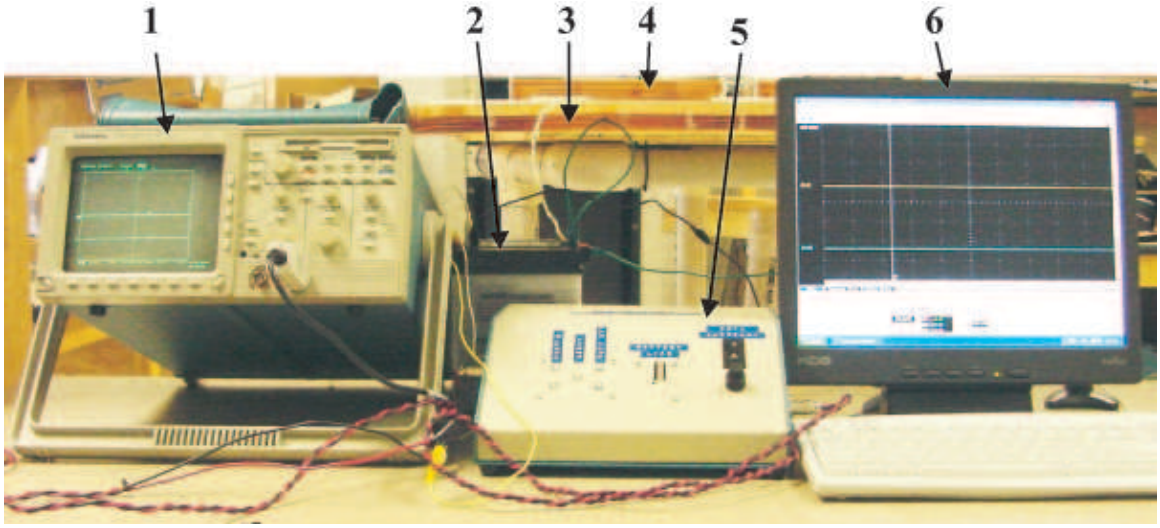

Figure 3.4: Hardware configuration of pulsed EMI system. (1) Oscilloscope (2) DC power supply for pulser (3) Transmit coil (4) Receive coil (5) Pulser (6) Gagescope

3.3 Transmitter and Receiver Coil Characteristics

The transmitter and receiver coil pair used in the measurements is presented in Figure 3.6. The 1m×1m transmitter coil consists of 10 turns of 18 AWG magnetic wire. Each 0.33m×0.33m coil of the figure-8 receiver consists of 14 turns of 18 AWG magnetic wire. Square coils were chosen because they are easier than round coils to construct. The receiver coils are glued to a Plexiglas sheet that is designed to slide atop another Plexiglas sheet that has been glued to the top of the transmitter coil frame. While transmitting over the band of frequencies of interest, the receiver coil output voltage is minimized by carefully positioning the receiver coil with respect to the transmitter coil.

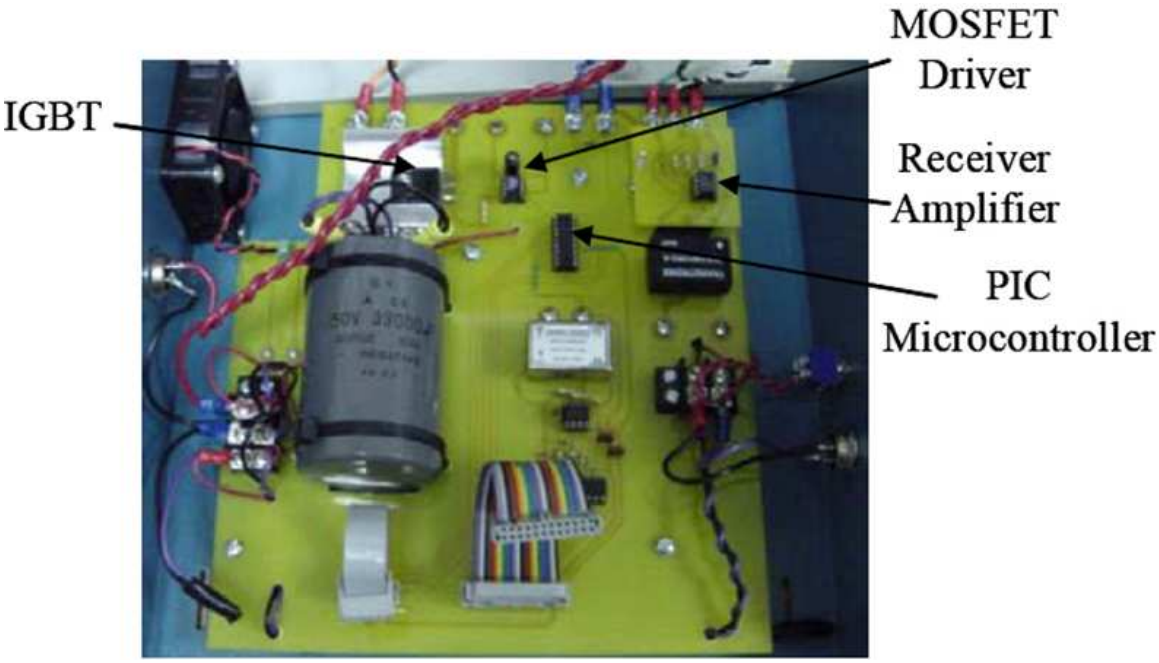

Figure 3.5: Components of the pulser on a printed circuit board

3.3.1 Various Trade-offs Considered in Coil Construction

The response of an EMI system not only depends on the physical and material characteristics and the location of the target, but also on the characteristics of the transmitter and receiver coils. There are many tradeoffs that must be addressed regarding coil design some of which are described in the next section.

Coil Dimensions

A good coil design requires trade-offs among competing objectives. For example, Figure 3.7 plots the magnetic field along the axis (z-axis) of a square loop for side of 10, 25, 50 and 100cm ($H_Z = Ia^2/\left[2\pi\left(h^2 + a^2/4\right)\sqrt{h^2 + a^2/2}\right]$, $I = 1$ ampere). The magnetic field at the center of the loop (z=0) decreases with increasing loop size, but the magnetic field along the axis of a large loop diminishes more slowly than that of a smaller loop. Therefore, transmitter coil dimensions are chosen as 1m×1m to provide

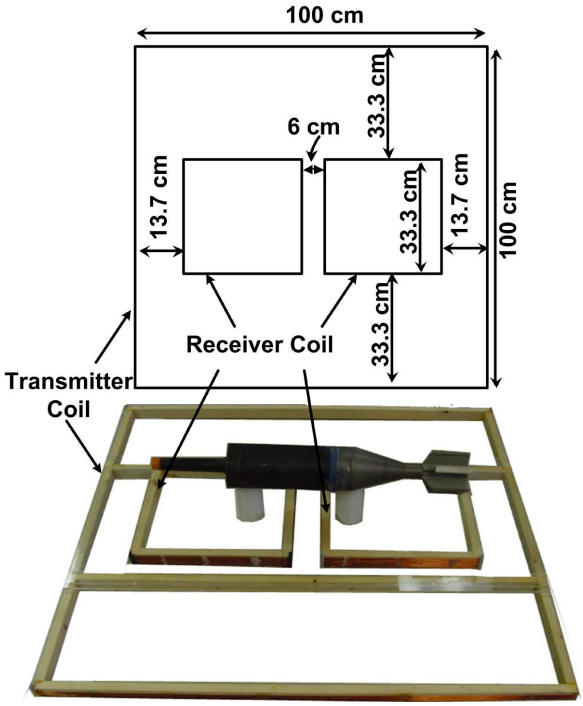

Figure 3.6: Transmitter and receiver coil pair used in CW and pulsed EMI measurements

good depth sensitivity without sacrificing system sensitivity to close-in (close to the plane of the coils) sensitivity.

Direct Coupling

Direct coupling between the transmitter and the receiver coils is another setback in the measurements as the direct coupled signal can be much larger than the object response and therefore may mask the weak object response. For this reason, the receiver is chosen to be wound in a bucking fashion where two coils with equal number of turns and of opposite polarity are connected in series. Equal flux passing through each coil that theoretically cancel. The dimensions of each of the two receiver coils is 0.33m×0.33m. Note that a bucking configuration can be used on the transmitter instead of receiver and GEM-3 sensor sold by Geophex is an example of an EMI

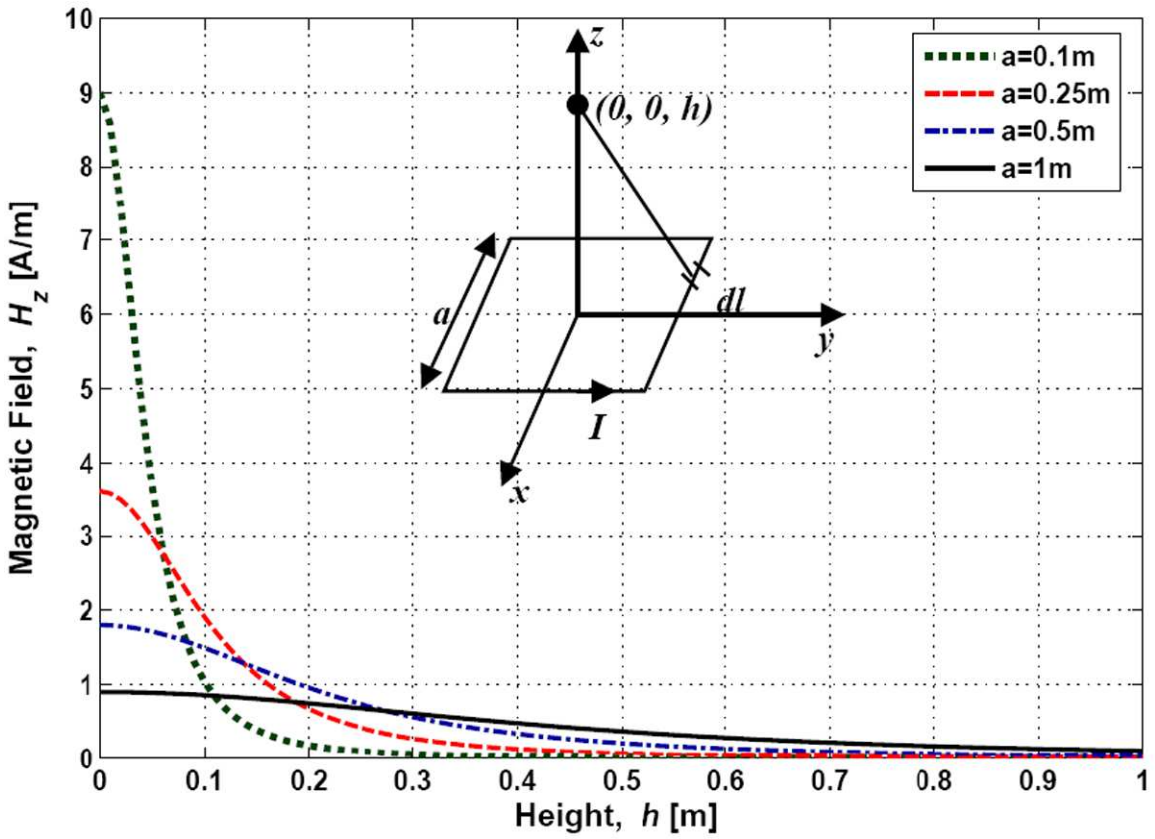

Figure 3.7: Magnetic field along the axis (z-axis) of a square loop for side of 10, 25, 50 and 100cm

sensor that utilizes just such configuration [58]. Another approach commonly used in pulsed system is to wait until the transmitter current falls below the noise level to acquire the object response. Once the transmitter current decays sufficiently the captured response will be due only to the object.

Sensitivity Maps

One way to evaluate the sensor coil pair without involving the target characteristics is by static sensitivity maps as first introduced by Silvester [59]. "The static sensitivity can be interpreted physically as the ratio of open-circuit output voltage change to the input voltage, per unit volume of perfectly conducting sphere, assuming

the sphere to be infinitesimally small and the coils to consist of one turn each" [59]. And, static sensitivity is directly proportional to $\mathbf{H_T} \bullet \mathbf{H_R}$, where $\mathbf{H_T}$ and $\mathbf{H_R}$ are the magnetic fields due to transmitter and receiver coils respectively and each can be computed using the Bio-Savart Law. Figure 3.8 presents the sensitive maps corresponding to a 1m×1m transmitter coil and 0.33m×0.33m figure-8 receiver coil pair superimposed on a line diagram of the sensor coils. The plots are over the x-y plane at various heights and the dot ($x \approx$0.2m, $y = 0$,z) represents the center of one coil of figure-8 receiver. The contours represent sensor sensitivity in dB (where 0dB corresponds to the maximum sensitivity).

Important observations made from these sensitivity maps are

1. The sensitivity is minimum at the center of the sensor ($x = 0$, $y = 0$) as the fields cancel out due to the symmetry of the figure-8 receiver.

2. For small z, the point of maximum sensitivity is at the center of each coil ($y = 0$ and $x \approx \pm$ 0.2m) of figure-8 receiver and drifts away from the center (dot) as z increases.

3. With a 10cm increase in z the sensitivity diminishes by ∼10dB at the center of receiver coil (dot).

Optimal Number of Transmitter Coil Turns for V_{OUT}/V_S Measurement

Another trade-off in coil design exists between system bandwidth and gain, both of which depend on the number of transmit coil turns N_T. In section 2.3, the frequency-domain transfer function of a conducting loop is determined by solving a magnetically coupled circuit representation of an EMI system. In this section, the

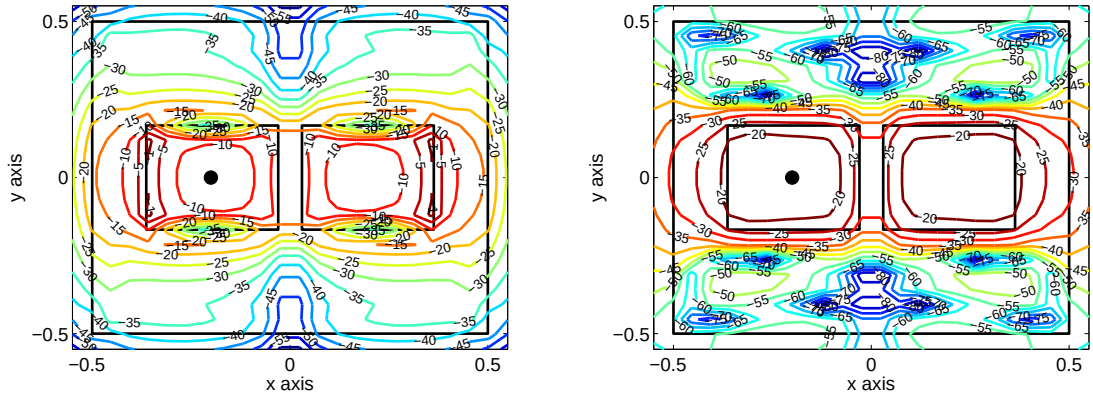

(a) z = 1 cm

(b) z = 10 cm

(c) z = 20 cm

(d) z = 50 cm

Figure 3.8: Static sensitivity maps superimposed on a line diagram of the EMI sensor. Plots over -0.5m ≤ x ≤ 0.5m, -0.5m ≤ y ≤ 0.5m at z = 1, 10, 20, 50cm

physical characteristics of the transmitting coil are included in the aforementioned analysis. Referring to Figure 2.2(a), the object current of equation (2.1) can be rearranged as

$$I_O = -\frac{j\omega M_{TO}}{(R_O + j\omega L_O)} I_T \tag{3.1}$$

where transmitter current I_T is the source voltage divided by the transmitter coil impedance

$$I_T = -\frac{V_S}{(R_T + j\omega L_T)} \tag{3.2}$$

Substituting equation (3.2) in equation (3.1) yields

$$I_O = -\frac{j\omega M_{TO} V_S}{(R_O + j\omega L_O)(R_T + j\omega L_T)} \tag{3.3}$$

The receiver current is given by

$$I_R = -\frac{j\omega M_{OR}}{(Z_R + R_R + j\omega L_R)} I_O \tag{3.4}$$

Eliminating I_O in the above equation results in

$$I_R = \frac{-j\omega M_{OR} j\omega M_{TO} V_S}{(Z_R + R_R + j\omega L_R)(R_O + j\omega L_O)(R_T + j\omega L_T)} \tag{3.5}$$

The output voltage is the product of the receiver current, I_R and the load impedance Z_R and is given by

$$V_{OUT} = -\frac{Z_R j\omega M_{OR} j\omega M_{TO} V_S}{(Z_R + R_R + j\omega L_R)(R_O + j\omega L_O)(R_T + j\omega L_T)} \tag{3.6}$$

The system transfer function V_{OUT}/V_S is then given by

$$\frac{V_{OUT}}{V_S} = -\frac{Z_R j\omega M_{OR} j\omega M_{TO}}{(Z_R + R_R + j\omega L_R)(R_O + j\omega L_O)(R_T + j\omega L_T)} \tag{3.7}$$

First assuming that the receiver coil is open circuited, i.e., $Z_R = \infty$, equation (3.7) reduces to

$$\frac{V_{OUT}}{V_S} = -\frac{j\omega M_{OR} j\omega M_{TO}}{(R_O + j\omega L_O)(R_T + j\omega L_T)} \tag{3.8}$$

If the object and transmitter coil radian break frequencies are defined to be $\omega_O = R_O/L_O$ and $\omega_T = R_T/L_T$ respectively, equation (3.8) can be expressed as

$$\frac{V_{OUT}}{V_S} = -\frac{M_{OR}M_{TO}}{L_T L_O}\frac{j\omega/\omega_T}{(1 + j\omega/\omega_T)}\frac{j\omega/\omega_O}{(1 + j\omega/\omega_O)} \tag{3.9}$$

The high-pass filter (frequency dependent) terms in equation (3.9) are associated with the transmitter coil (ω_T) and object (ω_O) in the same order. For a high-pass filter, it can be noticed from Figure 3.9 that for operating frequencies above the break frequency the magnitude of the response approaches unity (0dB), at the break frequency is 3dB below ($1/\sqrt{2}$ times) its high frequency asymptote Furthermore, the response decreases by a factor of 10 (20dB) per decade decrease in frequency. The phase starts at 90° close to DC, is 45° at the break frequency and asymptotes to 0° for frequencies well above the break frequency.

The transmitter coil resistance R_T is proportional to N_T and inductance L_T is proportional to N_T^2 resulting in a transmitter coil break frequency ($\omega_T = R_T/L_T$) that is inversely proportional to N_T. The transmitter coil resistance is R_{coil}=917mΩ

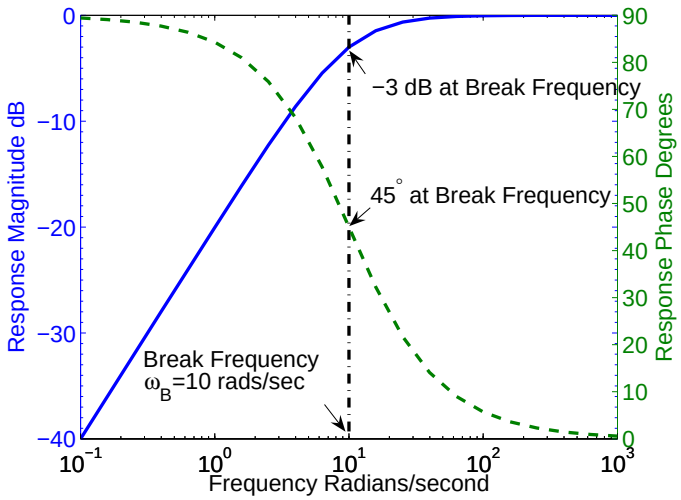

Figure 3.9: Transfer characteristics of a high-pass filter: $(j\omega/10)/(1+j\omega/10)$. Solid line is the magnitude response and dashed line is the phase response

and its inductance is L_{coil}=357μH (measured at 1kHz). Therefore 3dB break frequency of the coil is approximately 400Hz. At 4Hz the overall system response is attenuated by 40dB compared to what it would be if this coil had enough turns to drop the break frequency by two decades.

Certainly, the system would be improved in terms of bandwidth if N_T is increased to shift the transmitter coil break frequency close to the lowest frequency of interest; however, there is an important trade-off to be considered. V_{OUT}/V_S of equation (3.9) is proportional to $M_{OR}M_{TO}/L_TL_O$ which in turn is proportional to $\sqrt{L_R/L_T}$ (since, $M_{ij} = k_{ij}\sqrt{L_iL_j}$). Therefore, V_{OUT}/V_S is proportional to N_R/N_T. So, for a fixed number of receiver coil turns N_R, the amplitude of the response decreases with increase in N_T. N_R can be increased along with N_T to maintain the amplitude, but this will lead to additional more trade-offs that are addressed subsequently.

Receiver Coil and Receiver Coil Amplifier Considerations for V_{OUT}/V_S Measurement

The weak signals induced in the receiver coil by the eddy currents in the buried metallic object are boosted using an operational amplifier shown in Figure 3.10. It is

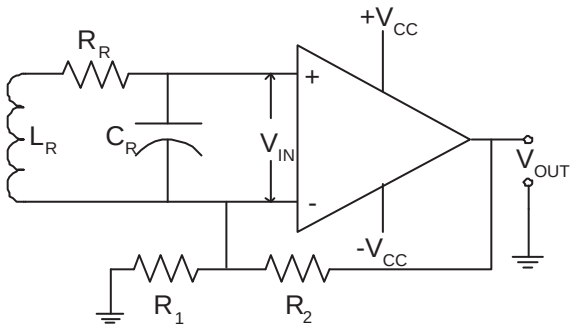

Figure 3.10: Operational amplifier connected in a noninverting configuration to the receiver coil. The parasitic capacitance of the receiver coil distorts measurements of the object's response.

connected in a noninverting configuration and provides a voltage gain $V_{OUT}/V_{IN} = 1 + R_2/R_1$. In noninverting configuration the operational amplifier has a very large (many mega ohms) input impedance. Because of this, currents will begin to flow through the parasitic capacitance C_R above a certain frequency. Due to the resonant circuit formed by L_R, R_R and C_R the input voltage V_{IN} will increase proportional to frequency at 20dB/decade up to the first self-resonance of the receiver coil (typically around 10kHz) which will in turn distort the output voltage and make it difficult to recover the object response. Equivalently, the transfer function (equation (3.9)) is now multiplied by a new frequency dependent factor that takes into account the resonant nature of the receiver coil

$$\frac{\omega_n^2}{s^2 + 2\varsigma\omega_n s + \omega_n^2} \tag{3.10}$$

which is a closed-loop transfer function for the standard second-order system where the natural resonant frequency $\omega_n = 1/\sqrt{L_R C_R}$ and the damping constant $\varsigma = 0.5 R_R \sqrt{L_R C_R}$. The resulting system transfer function becomes

$$\frac{V_{OUT}}{V_S} = -\frac{M_{OR} M_{TO}}{L_T L_O} \frac{j\omega/\omega_T}{(1 + j\omega/\omega_T)} \frac{j\omega/\omega_O}{(1 + j\omega/\omega_O)} \frac{\omega_n^2}{s^2 + 2\varsigma\omega_n s + \omega_n^2} \left(1 + \frac{R_2}{R_1}\right) \quad (3.11)$$

The resonance effect of the receiver coil can be avoided by measuring the current in the receiver coil (instead of the voltage) and using a current-to-voltage converter [60], [61].

Optimal Number of Transmitter Coil Turns for Object Current Measurement

The case in which the object current I_O is measured (instead of the voltage proportional to the object response) is considered in this section. Rearranging the terms in equations (3.1) and (3.2) yields

$$I_O = -\frac{M_{TO}}{L_O} \frac{j\omega/\omega_O}{(1 + j\omega/\omega_O)} I_T \quad (3.12)$$

and

$$I_T = -\frac{V_S/R_T}{(1 + j\omega/\omega_T)} \quad (3.13)$$

Since there is no extra $j\omega$ term in equation (3.13), I_T is a single pole low pass filter. Hence, the transmitter coil break frequency should be much higher than that of object $\omega_T >> \omega_O$. As ω_T is inversely proportional to N_T, theoretically it appears to be

desirable to use as few turns as possible so that the transmitter coil impedance is low enough so that transmitter amplifier can supply rated current. However practically speaking, a reduced number of transmitter coil turns decreases the field strength at the target thereby weakening the overall response. Note that more transmitter turns can be used to improve the field strength if a resistor is added in series with the transmitter. However, a series resistor will reduce the current through the transmitter coil which but can be overcome by using a more powerful amplifier. In short, a large number of transmitter coil turns along with a series resistor and increased power can be used to achieve both bandwidth and sensitivity.

Receiver Coil and Receiver Coil Amplifier Considerations for Object Current Measurement

The operational amplifier shown in Figure 3.11 is connected in an inverting configuration (input into negative terminal) as a current-to-voltage converter, so that $V_{OUT} = I_R R_F$ where I_R is the receiver coil current and R_F is the feedback resistor that sets the gain.

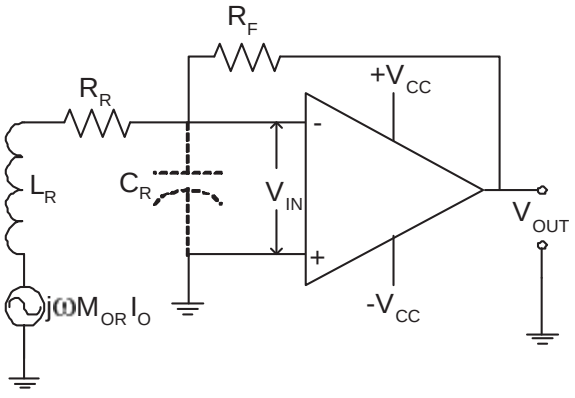

Figure 3.11: Operational amplifier connected in an inverting configuration to the receiver coil as a current-to-voltage converter.

The voltage induced in the receiver coil due to object eddy currents is given by $j\omega M_{OR} I_O$. Receiver current I_R is induced voltage divided by the receiver coil impedance

$$I_R = \frac{j\omega M_{OR} I_O}{R_R + j\omega L_R} = \frac{M_{OR}}{L_R} \frac{j\omega/\omega_R}{1 + j\omega/\omega_R} I_O \tag{3.14}$$

As the receiver coil break frequency is $\omega_R = R_R/L_R$, the operational amplifier output voltage may be written as

$$V_{OUT} = R_F I_R = R_F \frac{M_{OR}}{L_R} \frac{j\omega/\omega_R}{1 + j\omega/\omega_R} I_O \tag{3.15}$$

Manipulation of equations (3.12), (3.13) and (3.15) yields an object response

$$\frac{V_{OUT}}{V_S} = \frac{R_F}{R_T} \left(\frac{M_{TO} M_{OR}}{L_O L_R} \right) \left(\frac{1}{1 + j\omega/\omega_T} \right) \left(\frac{j\omega/\omega_O}{1 + j\omega/\omega_O} \right) \left(\frac{j\omega/\omega_R}{1 + j\omega/\omega_R} \right) \tag{3.16}$$

which is undistorted over the range of frequencies from ω_R to the first resonance frequency of the receiver coil. Once the transmitter has been developed as explained in previous section and the coil dimensions of the receiver have been determined, the number of receiver coil turns should be chosen to fix the 3dB frequency to ω_R.

In the development of equation (3.15) the effect of the parasitic capacitance C_R is ignored as the input impedance of the current-to-voltage converter is negligible..

3.4 Summary

In this chapter laboratory setups of CW and pulsed-EMI systems are described and several factors affecting system design have been described. Most importantly,

using a current-to-voltage converting operational amplifier to measure the "short-circuit" receiver coil current allows one to avoid problems introduced by parasitic capacitance.

Chapter 4

Measurements

4.1 Introduction

Time- and frequency-domain EMI responses of UXO-like ferrous targets acquired using the systems described in Chapter 3 are presented. The measured responses are validated by comparing them with numerical simulations. Effects of target size, wall thickness, and the presence of copper bands on the response characteristics are discussed. Special attention is given to the target response characteristics at extremely low frequencies or equivalently very late times. The next chapter presents a quantitative measure of discrimination performance enhancement provided by extremely low frequency target and late-time features

4.2 Test Targets

Figure 4.1 shows the ferrous cylinders used for simulations and measurements. The cylinders are of four different sizes and three different wall thicknesses and the copper bands model the driving bands on real UXO. The number on each cylinder represents its size and the letter represents its wall thickness. The dimensions of these twelve cylinders are given in table 4.1.

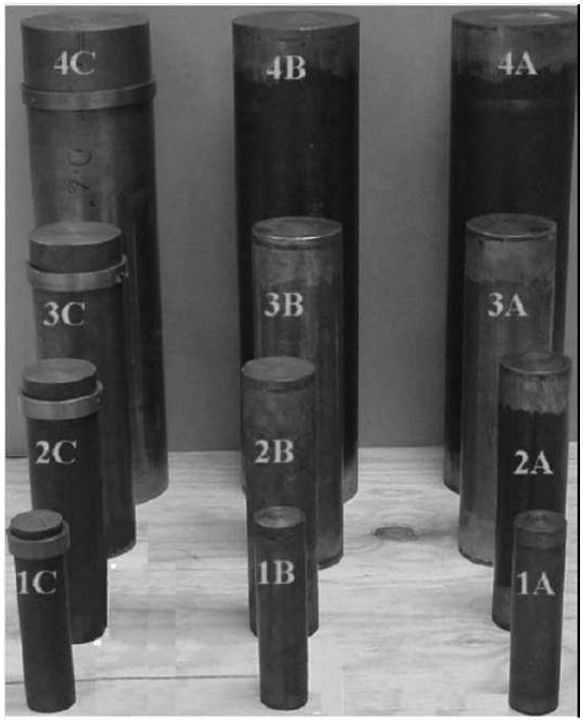

Figure 4.1: Test targets used in the measurements.

Table 4.1: Size details of the test targets

Target	Wall Thickness (in)	L (in)	D (in)
1A	1/4	8	2
1B	1/2	8	2
1C	Solid	8	2
2A	1/4	12	3
2B	1/2	12	3
2C	Solid	12	3
3A	1/4	16	4
3B	1/2	16	4
3C	Solid	16	4
4A	1/4	24	6
4B	1/2	24	6
4C	Solid	24	6

4.3 Frequency-Domain Measurements

The CW system presented in Figure 3.2 is used to acquire the frequency responses of the targets. Results presented here are for axial excitation of the target (i.e., vertical orientation of target with respect to the sensor).

4.3.1 Comparison between FEM and Measured Responses

Due to lack of three-dimensional symmetry, the finite cylinder does not have an analytical solution and therefore, a numerical method has to be employed to determine its scattered field. In this work, the Finite Element Method (FEM) model developed by Faircloth is chosen to pursue a direct numerical computation of the body-of-revolution (BOR) response for axial excitation [57]. Good agreement between the analytical and FEM computed response for the sphere is demonstrated. As the error in the FEM results is negligible, a least squared error minimization algorithm is used to effectively normalize the measured data with respect to the FEM results for comparison purposes. Excellent agreement between measurements and FEM simulation were achieved when the conductivity and permeability of the ferrous cylinders were taken as 5.82×10^6 S/m and 70 respectively. The normalized FEM and measured responses of cylinder 1B with a centered copper driving band are compared in Figure 4.2. Note that the results are in close agreement as anticipated.

4.3.2 Effect of Target Size

To evaluate the importance of extremely low-frequency response of UXO-like targets, an initial comparison of steel cylinders of varying size was performed. Figure 4.3 shows normalized responses of solid cylinders for all four sizes. Clearly, the overall

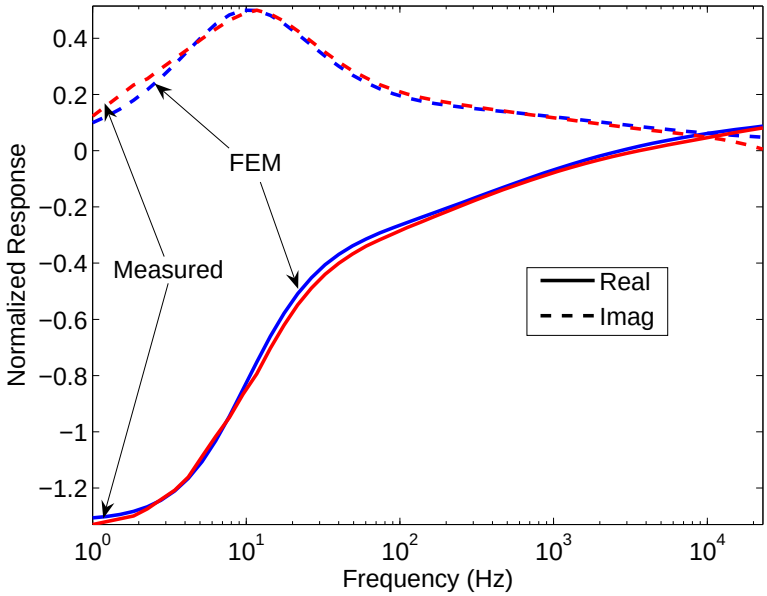

Figure 4.2: Comparison of response obtained by FEM and measurements for 1B cylinder with centered copper ring.

trends of the responses are quite similar with the exception of a downward frequency shift of the low-frequency real asymptote and quadrature peak with increasing cylinder size. In particular, note that the in-phase responses of cylinders 1C and 2C start approaching their low-frequency limit around 1Hz and due to higher metallic content of cylinders 3C and 4C, their responses tend to their low-frequency asymptotes at frequencies below 1Hz.

The frequency range for FEM simulation is extended downward to 1mHz in order to study the target response behavior at extremely low frequencies. Figure 4.4 compares FEM responses for different sized steel cylinders. The FEM responses shown in Figure 4.4 displays the same trends as the measured response of Figure 4.3. Of particular interest is the fact that none of the cylinders reach their in-phase low-frequency asymptotic limit until well below the typical EMI frequency band (30Hz to

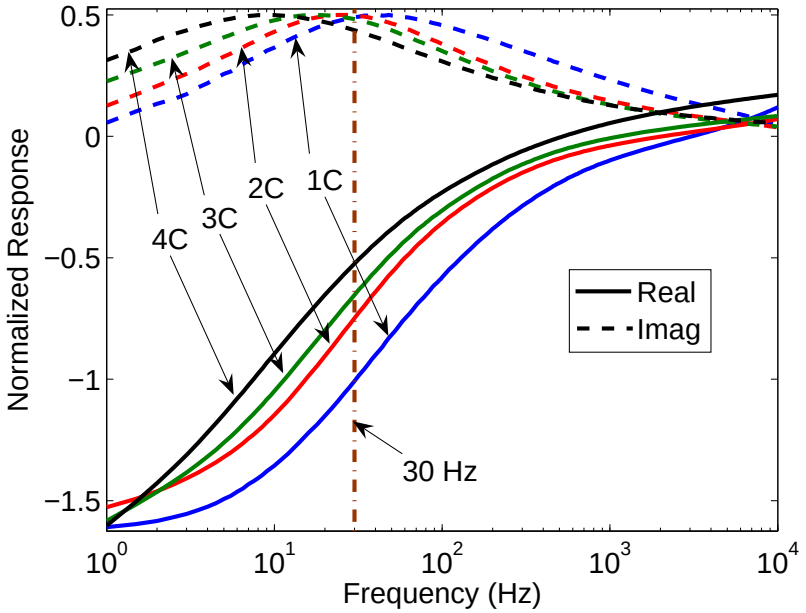

Figure 4.3: Measured responses of four solid steel cylinders of varying size.

24kHz). Since each of the cylinders has its own unique point at which the asymptotic limit is reached, valuable discrimination information is neglected if one collects data only in the 30Hz to 24kHz range. Figure 4.5 gives a detailed view of the low-frequency asymptotic behavior of the real part of the response for different size cylinders. The low frequency asymptote of the largest cylinder (4C) is not reached until ∼10mHz which is well below the lowest operating frequency of commercially available CW EMI systems. Similarly, the asymptote of the smallest cylinder (1C) is not reached until ∼300mHz which is two decades below the lowest operating frequency (30Hz) of commercial systems.

4.3.3 Effect of Wall Thickness

Next, the effect of wall thickness on target response is compared for a variety of cylinders. Figure 4.6 shows the measured response of three "2 Series" cylinders that

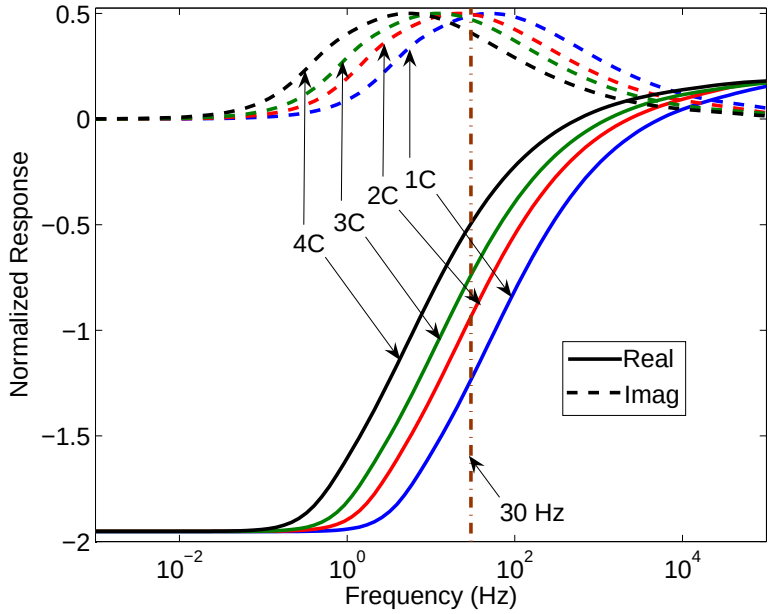

Figure 4.4: FEM Response of four solid steel cylinders of varying size.

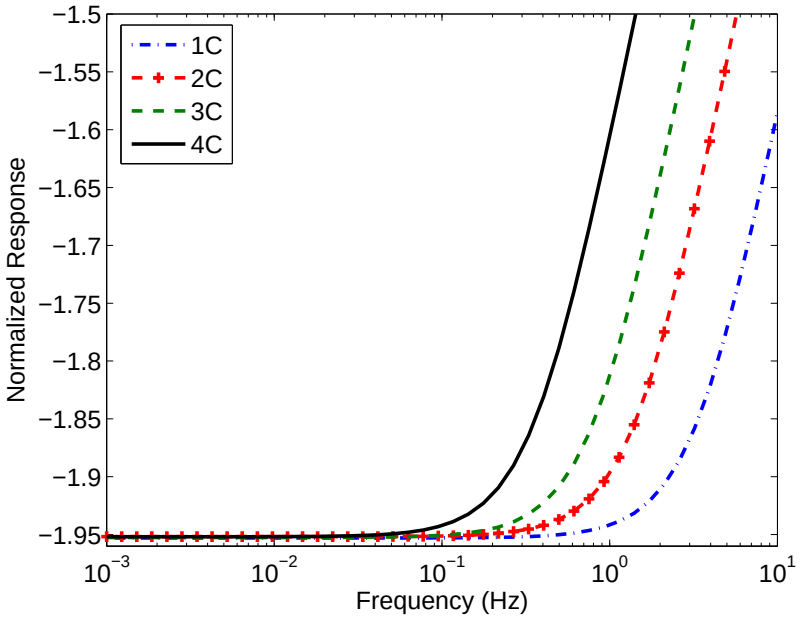

Figure 4.5: Extremely low frequency FEM response of the four solid steel cylinders

have different wall thicknesses. A line at 30Hz divides the figure into low-frequency

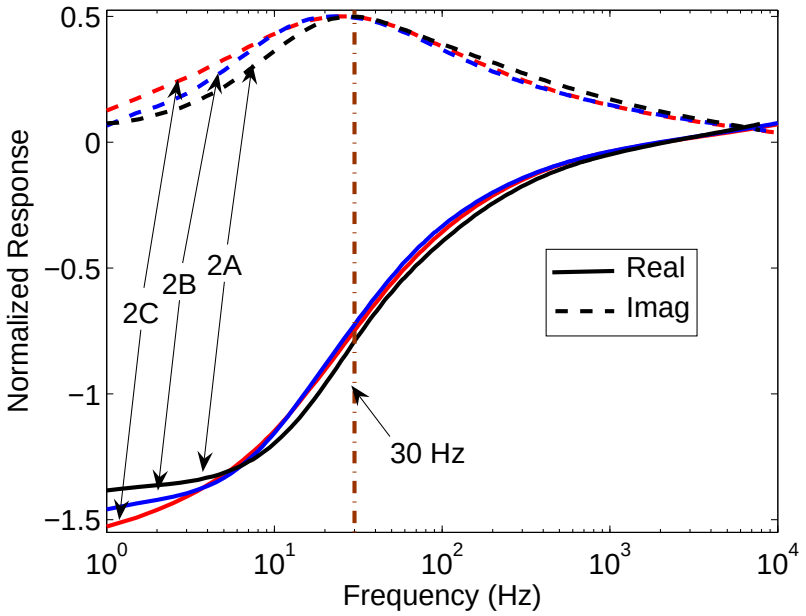

Figure 4.6: Measured responses of visually identical steel cylinders with differing wall thicknesses

band and typical EMI band. Above 30Hz, there is very little difference between the responses of the three cylinders. Therefore, discrimination using only the information above 30Hz would prove most difficult at low SNRs. However, below 30Hz, there is a notable difference among the responses.

FEM responses of cylinders 2A, 2B and 2C for the frequencies from 1mHz to 100kHz are presented in Figure 4.7. FEM responses show the same trends as determined from the measured responses presented in Figure 4.6. Once again, the difference in the responses is only significant below 30Hz. Another point to be noted here is that the imaginary part of all the three responses asymptote to zero while the real part asymptotes to a distinct negative value, just as in the analytical hollow

sphere case shown in Figure 2.9. It is clear from Figure 4.8 that the thin-walled cylinder reaches its low-frequency asymptote at ∼1Hz whereas the other cylinders have asymptotes below ∼200 mHz. Obviously, the low-frequency information should be helpful in discerning UXO-like targets from flat plates or other thin metallic debris.

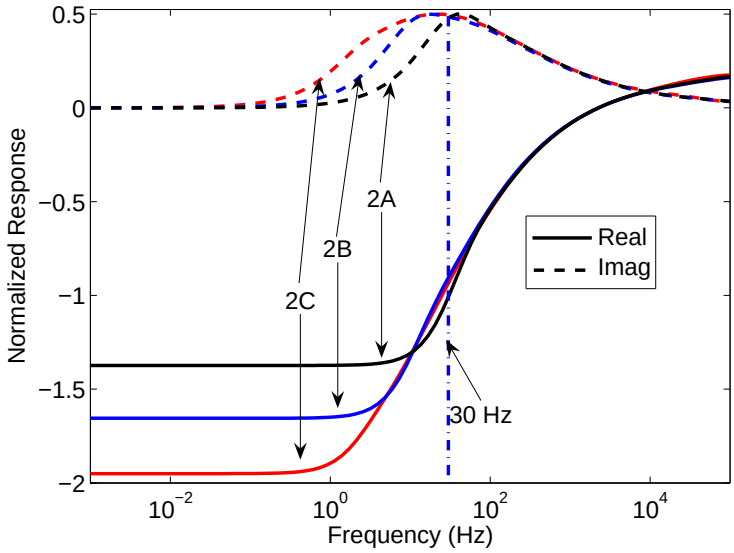

Figure 4.7: FEM response of visually identical cylinders.

4.3.4 Effect of Driving Bands

Actual UXO targets are often equipped with metallic rings known as driving bands. The bands are usually made of highly conductive, non-permeable metals such as copper. For the vertical (axial) excitation, presence of the driving band should significantly affect the response of a target. The effect of centered copper driving band on ferrous cylinder response is presented in Figures 4.9 and 4.10 using measured responses and FEM simulated data. When a copper driving band is placed around the cylinder its quadrature peak shifts down in frequency. The most significant fact is that the quadrature peak of the banded case is now well below the 30Hz lower

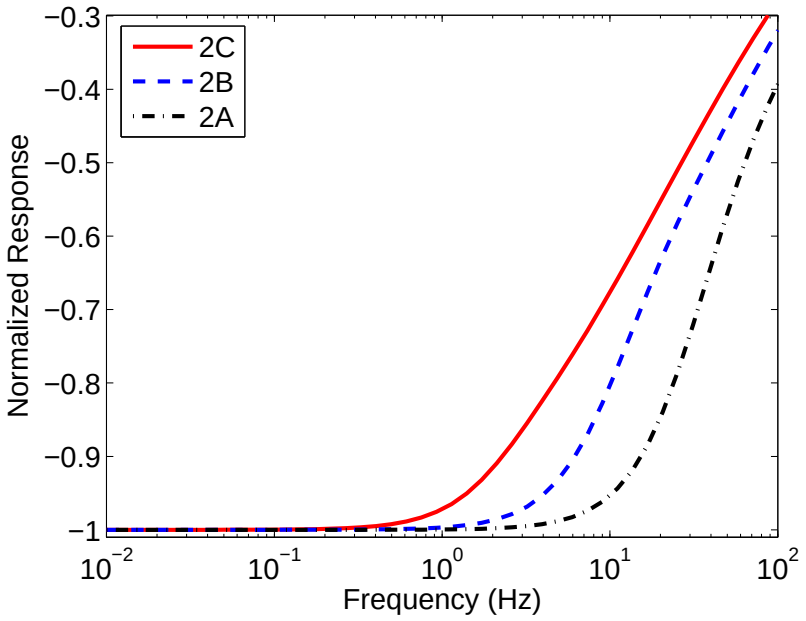

Figure 4.8: Low frequency FEM response of visually identical cylinders.

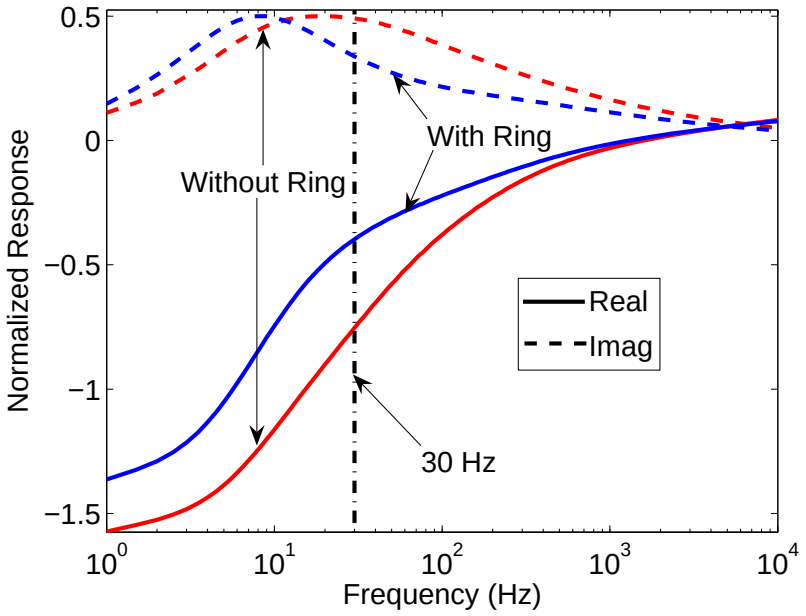

Figure 4.9: Effect of driving band on targets Measured response.

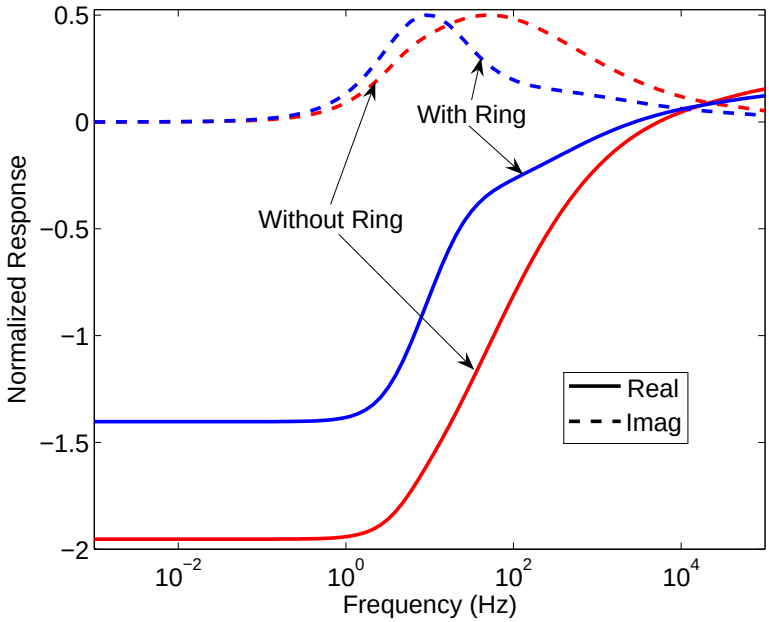

Figure 4.10: Effect of driving band on targets FEM response.

limit of typical EMI measurement systems. Using only the typical EMI measurement spectrum could adversely affect discrimination performance since quadrature peak frequency is used as a parameter in discrimination algorithms [38].

4.3.5 UXO Measurements

Figure 4.11 shows three UXO targets that are measured with the incident magnetic field along the long axis of the targets. Figure 4.12 presents the responses of these three UXOs in the 1Hz to 10kHz range. Note that the data in this range does display the expected low-frequency asymptotic behavior (e.g. - the real part converges to a constant negative value and imaginary part converges to zero). In general the response of the UXOs is similar to that of the test cylinders.

Figure 4.11: UXO items from left to right 155mm, 105mm, and 107mm shell

4.4 Time-Domain Measurements

A comparison of theoretical, FEM, and measured time-domain response of an 18 AWG 5" copper loop is presented in Figure 4.13. It can be seen from the figure that the measured time responses are in close agreement with FEM and theoretical results.

Figure 4.14 shows the measured time-domain response of the "2 series" (3" diameter $\times$ 12" height) cylinders with same diameter and height but different wall thicknesses. The response has a steep slope in early time and a gradual slope later. The early time response corresponds to higher frequencies that do not penetrate the object. Therefore, the responses of the three cylinders are almost identical in early time. As the fields penetrate deeper into the object at late time (low frequencies), the response reveals information regarding the target's inner geometry. The late time target information can be used to improve discrimination performance. However, it

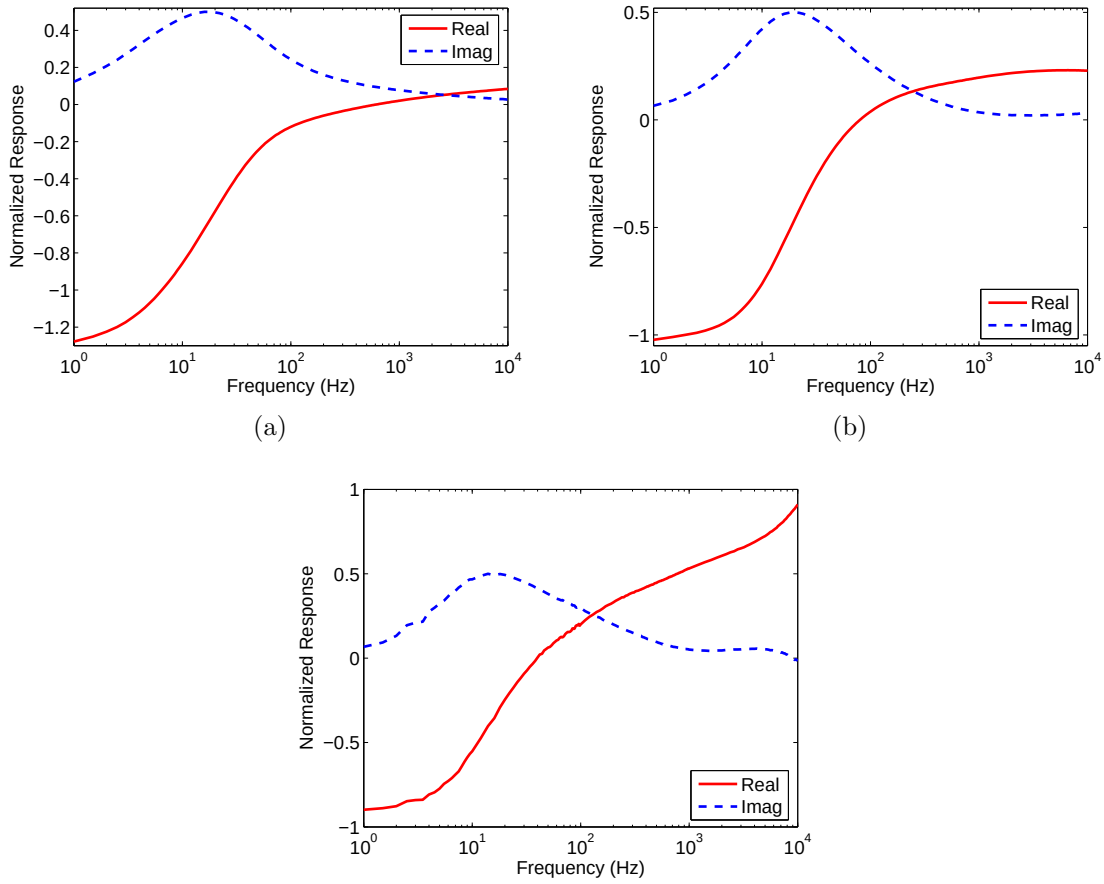

Figure 4.12: Measured Response of (a) 155 mm shell (b) 105 mm shell (c) 107 mm shell in the 1Hz to 10kHz frequency range.

is very difficult to measure the late time data as the magnitude of the signal falls below the noise level. Hence, only the data up to 17ms is shown in Figure 4.14. Improvements to the time-domain EMI system described in section 3.2.2 are currently underway to acquire late-time data beyond 17ms. In order to observe the nature of the response beyond 17ms, time-derivative of the FEM magnetic field responses are presented in Figure 4.15. The figure shows that there is a clear difference in the decay behavior depending on the wall thickness. The response of cylinder 2A decays faster and has a pure exponential decay starting at about 4ms. Whereas cylinder 2B goes

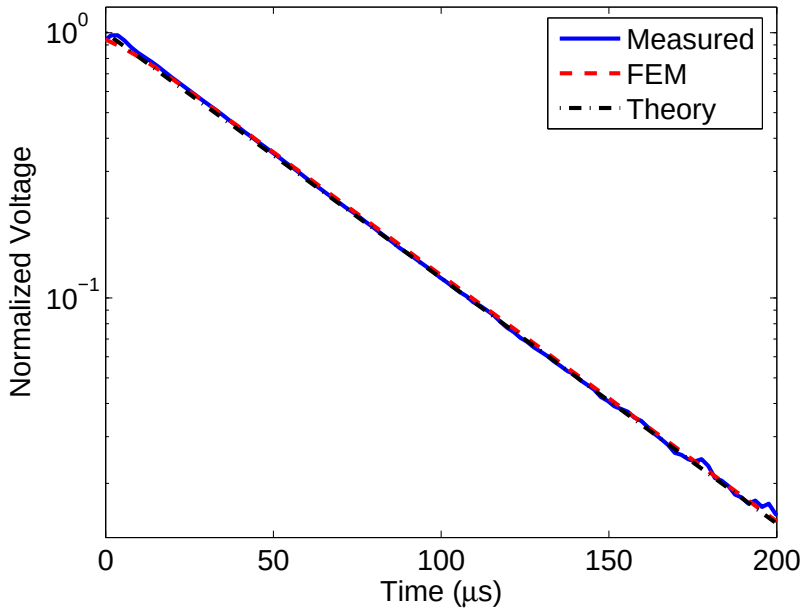

Figure 4.13: Theoretical, FEM and Measured Time-Domain response of 18 AWG 5" Copper loop

into a pure exponential regime at around 20ms and the exponential portion of the response for cylinder 2C would have been noticeable, if the response was extended beyond 40ms. Similar trends are observed in the cylinders of other series (1, 3 and 4) also.

Another interesting feature of the FEM data is the 'power-law to exponential transition' of cylinders with different dimensions but same wall thickness. Figure 4.16 presents the transient response of "A" cylinders (1/4″ wall thickness) of different sizes. As anticipated, the decay slows down with increase in the cylinder size, however, it can be noticed that all four cylinders enter a pure exponential regime at ∼4ms. Similarly, "B" cylinders (1/2″ wall thickness) are noticed to start decaying exponentially at ∼20ms. From the time responses presented in Figure 4.16 it can be inferred that the transition time is a characteristic of wall-thickness only (and not size).

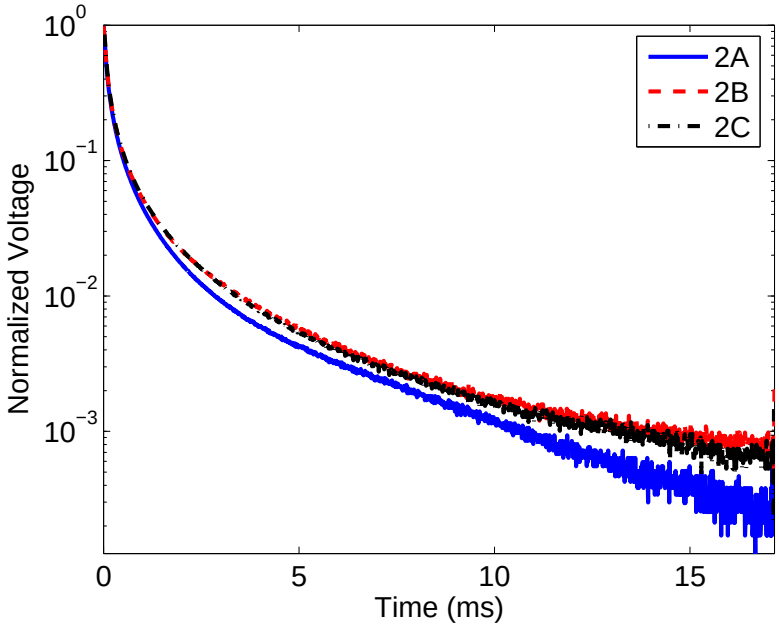

Figure 4.14: Measured decays for "2 series" cylinders identical except for wall thickness

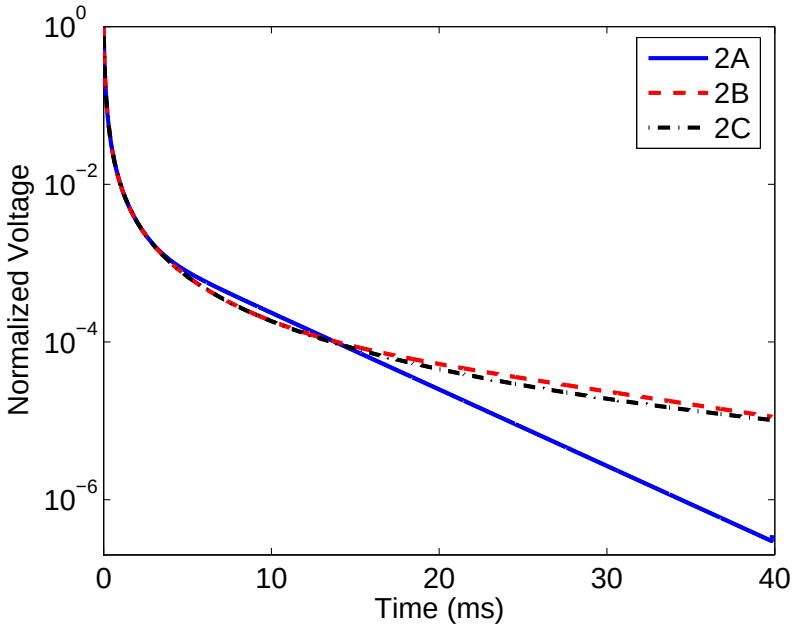

Figure 4.15: FEM decays for "2 series" cylinders identical except for wall thickness

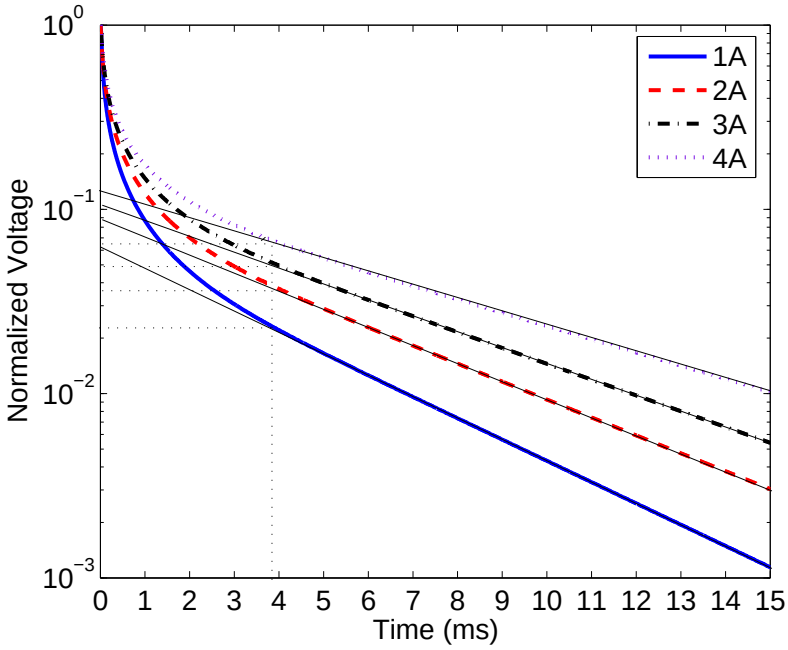

Figure 4.16: FEM decays for "A series" cylinders of different sizes and same wall thickness

It is important that of a time-domain EMI sensor be able to measure the transition from power-law to exponential decay. As seen in Figure 4.15, for cylinder "2C" this transition does not occur in the 0 to 40ms time window and it is very difficult to measure the data beyond 40ms. However, as mentioned earlier, transition from power-law to exponential decay (inflection time) is related to the quadrature peak of the frequency response which can be acquired with much greater ease using a frequency-domain EMI system.

The time-domain system was tested at Blossom Point Test field and currently efforts are continuing toward improving the system for sensitivity and duration of the acquisition. For further details readers are refered to [62].

4.5 Summary

Measured and FEM responses of cylinders in frequency and time-domain show that extremely low frequency or equivalently late-time data provides valuable target information which can improve discrimination relative to what can be achieved using the usual spectral content available from commercial systems. However, high fidelity low-frequency is easier to obtain with a CW system than a pulsed system. Discrimination improvement provided by ELF frequencies will be statistically analyzed in the next chapter.

Chapter 5

Statistical Analysis

5.1 Introduction

Chapters 2 and 4 show that frequency responses of UXO-size visually identical ferrous targets are not distinct until below 30Hz. Discrimination performance of an EMI system can be improved by extending the lower bound from 30Hz downward to 1Hz. A quantitative measure of improvement in discrimination performance provided by ELF data is presented in this chapter. Three statistical tests are analyzed using data in 1Hz to 24kHz and 30Hz to 24kHz ranges.

5.2 Noise Statistics

As noise characteristics are necessary to represent received the data set, noise is measured 150 times for frequencies over the entire 1Hz - 24kHz band. The noise distribution at each frequency point appears to be approximately Gaussian. The Gaussian assumption is confirmed by measuring the noise again this time 1000 times over the 1Hz to 100Hz range. The noise distribution at 1Hz and 100Hz based on the second measurement is shown in Fig. 5.1. Important observations are (i) noise is complex Gaussian, (ii) noise variance is frequency dependent and decreases with increasing frequency, and (iii) the variances of the real and imaginary parts at each frequency are approximately equal.

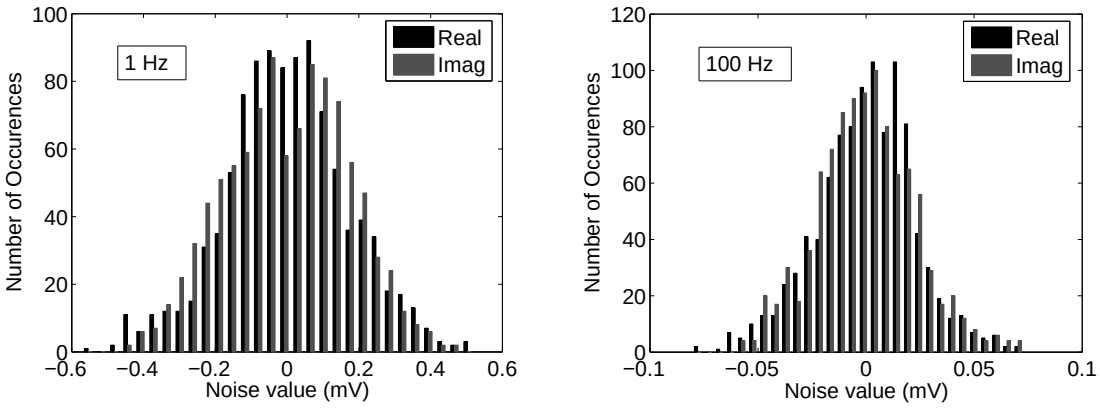

(a) (b)

Figure 5.1: Noise distribution at (a) 1Hz and (b) 100Hz

5.3 Discrimination Problem

Measured EMI responses of the twelve cylinders shown in Figure 4.1 were used for statistical analysis. Measurements taken with 50 averages provide high SNR data and forms the target library data set. Noise is added to the library data set in order to represent the received data set.

The received signal (or response), $r(f)$ is complex and is represented as

$$r(f) = y_i(f) + e(f) \qquad i = 1, 2, ..., N \tag{5.1}$$

where $y_i(f)$ is the expected response of the i^{th} cylinder and $e(f)$ is noise. As the data is not continuous and is obtained for M discrete frequencies, (5.1) can be written as

$$r_j = y_{ij} + e_j \qquad i = 1, 2, ..., N$$
$$j = 1, 2, ..., M \tag{5.2}$$

where $e_j \sim \mathcal{N}^C(0, \sigma_j^2)$ as explained in section 5.2. For simplicity, e_j's are assumed to be independent which implies that the r_j's are also independent.

Let error, z_j be defined as

$$z_j = r_j - y_{i_0 j} \qquad \begin{array}{l} i_0 = 1, 2, ..., N \\ j = 1, 2, ..., M \end{array} \tag{5.3}$$

where

$$z_j = \begin{cases} e_j & i = i_0 \\ (y_{ij} - y_{i_0 j}) + e_j & i \neq i_0 \end{cases} \tag{5.4}$$

And, the discrimination problem can be represented as a binary hypothesis problem where $\mathbf{z}$ is an observation, and alternate and null hypotheses are represented by

$$\begin{array}{rcl} H_0 & : & \text{Different target} \quad (i \neq i_0) \\ H_1 & : & \text{Same target} \quad (i = i_0) \end{array} \tag{5.5}$$

which is analogous to the 'no target' (null) and 'target' (alternate) hypotheses in a radar detection problem.

Three error functions are evaluated as a statistic for the decision rule involving the hypotheses defined in equation (5.5).

5.3.1 Square of Mean Error (SME)

According to a variant of the central limit theorem (CLT) [63], if Y_1, ..., Y_n, are n independent random variables each with probability density function $P_k(x_k)$, mean μ_k and variance σ_k^2, the distribution of sample mean of random variables (i.e.,

$\frac{1}{n}\sum_{k=1}^{n} Y_k$) rapidly approaches Gaussian distribution with a mean $\mu = \frac{1}{n}\sum_{k=1}^{n}\mu_k$ and a variance $\sigma^2 = \frac{1}{n}\sum_{k=1}^{n}\sigma_k^2$ as $n \to \infty$. Therefore, if $X_i = \frac{1}{M}\sum_{j=1}^{M} z_j$, then by the central limit theorem

$$X_i \overset{CLT}{\rightarrow} \begin{cases} \sim \mathcal{N}^C(0, \sigma^2) & i = i_0 \\ \sim \mathcal{N}^C(m_i, \sigma^2) & i \neq i_0 \end{cases} \tag{5.6}$$

where the variance σ^2 and mean m_i are given by

$$\begin{aligned} \sigma^2 &= \frac{1}{M}\sum_{j=1}^{M}\sigma_j^2 \\ m_i &= \frac{1}{M}\sum_{j=1}^{M}(y_{ij} - y_{i_0 j}) \end{aligned}$$

If a test target $\tilde{i_0}$ ($\tilde{i_0} = 1, 2, ..., N$) is picked and $X_{\tilde{i_0}}$ is calculated, then $\frac{2|X_{\tilde{i_0}}|^2}{\sigma^2}$ is $\mathcal{X}^2(2)$ (central chi-square function with two degrees of freedom) for $i_0 = \tilde{i_0}$. The test now can be defined as

$$\frac{2|X_{\tilde{i_0}}|^2}{\sigma^2} \underset{H_1}{\overset{H_0}{\gtrless}} \eta \tag{5.7}$$

where η is the threshold.

5.3.2 Mean Squared Error (MSE)

If X_i is defined as a sample mean of $|z_j|^2$ instead of a sample mean of z_j as in section 5.3.1, i.e., if $X_i = 1/M\sum_{j=1}^{M}|z_j|^2$, then again by central limit theorem,

$$X_i \overset{CLT}{\rightarrow} \begin{cases} \sim \mathcal{N}(\sigma^2, V_0) & i = i_0 \\ \sim \mathcal{N}(m_i, V_1) & i \neq i_0 \end{cases} \tag{5.8}$$

where

$$\begin{aligned}
\sigma^2 &= \frac{1}{M}\sum_{j=1}^{M}\sigma_j^2 \\
m_i &= \frac{1}{M}\sum_{j=1}^{M}(|y_{ij}-y_{i_0j}|^2) \qquad m_i \neq \sigma^2 \\
V_0 &= \frac{1}{M}\sum_{j=1}^{M}\sigma^2_{|e_j|^2} \\
V_1 &= \frac{1}{M}\sum_{j=1}^{M}(\sigma^2_{|e_j|^2}+4(y_{ij}-y_{i_0j})^2\sigma_j^2)
\end{aligned}$$

Therefore, if a test target $\tilde{i_0}$ ($\tilde{i_0} = 1, 2, ..., N$) is picked and $X_{\tilde{i_0}}$ is calculated, then $\frac{X_{\tilde{i_0}}-\sigma^2}{\sqrt{V_0}} \sim \mathcal{N}(0,1)$ (normal distribution). Hence, the test can be written as

$$\frac{X_{\tilde{i_0}}-\sigma^2}{\sqrt{V_0}} \underset{H_1}{\overset{H_0}{\gtrless}} \eta \tag{5.9}$$

5.3.3 Error-to-Noise Ratio (ENR)

If $\mathbf{z} = [z_1, z_2, ..., z_M]$ and $\mathbf{x} = [\mathrm{Re}(\mathbf{z}), \mathrm{Im}(\mathbf{z})]^T$, then a covariance matrix is defined as $\Sigma = diag(\sigma_x^2)$ and the statistic for this test is defined as $\mathbf{x}^T\mathbf{\Sigma}^{-1}\mathbf{x}$ which can also be written as $\sum_{j=1}^{2M}\frac{x_j^2}{\sigma_j^2}$. The test in this case can be written as

$$\mathbf{x}^T\mathbf{\Sigma}^{-1}\mathbf{x} \underset{H_1}{\overset{H_0}{\gtrless}} \eta \tag{5.10}$$

where η is the threshold. Note that $\mathbf{x}^T\mathbf{\Sigma}^{-1}\mathbf{x}$ has been used as a discriminant function for multivariate binary hypothesis problems [65] and multiple hypothesis problems [29].

The distributions of the three test statistics are presented in Figure 5.2.

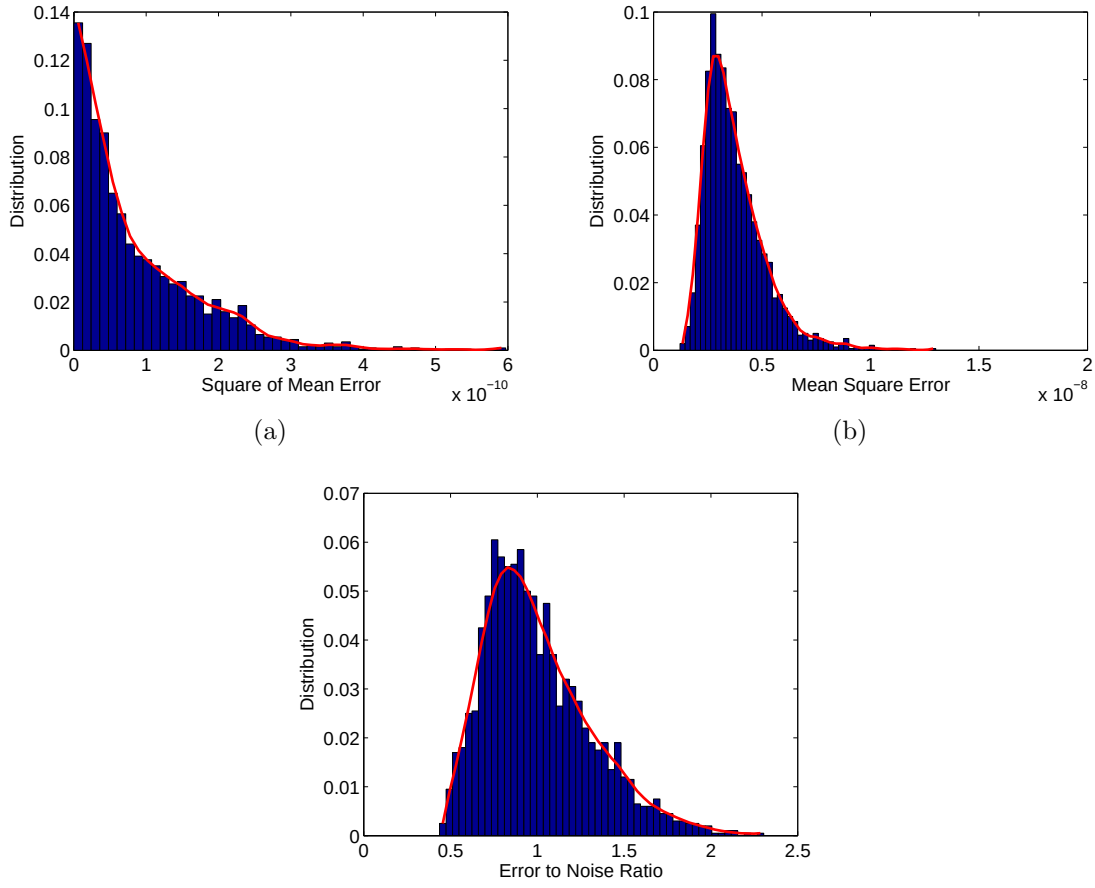

Figure 5.2: Distribution of test statistics (a) SME (b) MSE and (c) ENR

The expression for z_j in equation (5.3) is valid only if the target position is known. However, as the target depth is unknown, a series of measurements with the targets at various depths were performed, and the normalized responses were found to be the same. Therefore, to mitigate uncertainty due to the target depth, the received signal was normalized, and the new expression for r_j is given as

$$r_j = \frac{y_{ij}}{2(\mathbf{y_i})_{\mathbf{qp}}} + e_j \qquad i = 1, 2, ..., N \qquad j = 1, 2, ..., M \tag{5.11}$$

where $(\mathbf{y_i})_{\mathbf{qp}}$ is the quadrature peak. Then z_j is given by

$$z_j = r_j - \frac{y_{ij}}{2(\mathbf{y_i})_{\mathbf{qp}}} \qquad \begin{matrix} i = 1, 2, ..., N \\ j = 1, 2, ..., M \end{matrix} \tag{5.12}$$

Using normalized data changes the means and variances of the above-mentioned three methods, namely SME, MSE and ENR, but the decision rules in equations (5.7), (5.9) and (5.10) are still valid.

As shown in Figure 5.1, the noise variance is frequency dependent. So, signal-to-noise ratio (SNR) is defined at the quadrature peak and is given by

$$\text{SNR (dB)} = 10 \log_{10} \frac{(\mathbf{y_i})^{\mathbf{2}}_{\mathbf{qp}}}{\sigma^2_{\text{qp}}} \tag{5.13}$$

Figure 5.3 shows the performance of SME, MSE and ENR over restricted (30Hz to 24kHz) and extended (1Hz to 24kHz) bands in the presence of 22dB SNR. ENR performs better than other two methods because actual noise variance is included in ENR unlike mean of variances in SME and MSE.

As ENR performs the best of three methods, it is used to analyze the discrimination performance of the two frequency bands at different noise levels and is presented in Fig. 5.4. It can be noticed that for SNR above approximately 18dB, 1Hz to 24kHz band gives perfect performance and neither band performs well below -2dB. At a SNR of 8dB, for a probability of false alarm of 0.2, the probability of correct identification for 30Hz to 24kHz band is 0.6 and that for 1Hz to 24kHz is 0.9 - improvement by a factor of 1.5.

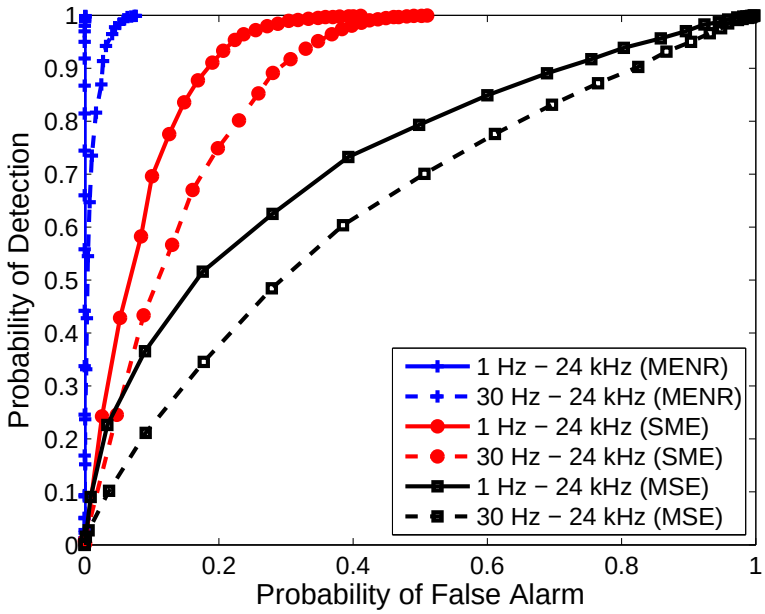

Figure 5.3: Performance of SME, MSE and ENR in for 22dB SNR over two frequency bands 30Hz to 24kHz and 1Hz to 24kHz

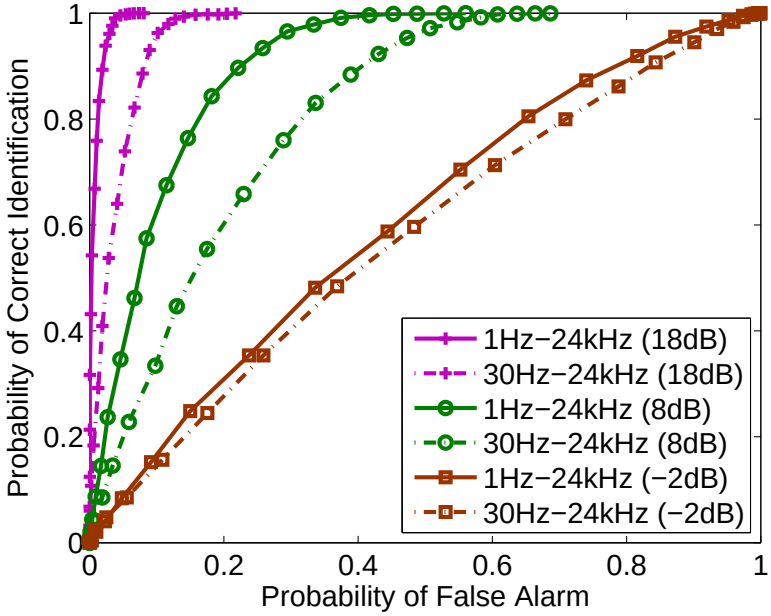

Figure 5.4: Comparison of the performance of 30Hz to 24kHz data and 1Hz to 24kHz data in identifying the cylinder correctly for three SNRs

5.4 Summary

In this chapter, the discrimination problem is defined as a binary hypothesis problem and noise characteristics are presented. Performance of three test statistics, SME, MSE and ENR is evaluated which shows that ENR performs the best due to the knowledge of noise. Performance of ENR for 8dB SNR shows that extended band performs 1.5 times better than the restricted band for 0.2 probability of false alarm.

Chapter 6

Conclusions

Even though there is a considerable (factor of 1.5) performance gain by using ELF band in CW systems, there is a price to pay for this improvement. It is time consuming to obtain very low frequency target data especially when many averages are required to achieve adequate SNR. For example, 100 averages at 1Hz will require at least 100 seconds which would also result in averaging over different orientations if the sensor is moving with respect to the target under test. One recognizes immediately, that it is not practical to operate a CW EMI system as a survey (towed or vehicular) sensor at very low frequencies. Alternatively, static measurements at predefined locations would eliminate sensor-motion noise as well as sensor location and orientation uncertainties [27]. In this "cued" approach, target locations would be marked using another detection technique (e.g. a simple total-field magnetometer) and the low frequency CW EMI system would be deployed to these known target locations for classification. An alternative deployment strategy is to use an EMI sensor operating in detection mode and shift to classification mode when a target is detected. This process will obviously lengthen the survey period but does not require intermediate marking for target reacquisition.

The research efforts presented is a first step towards showing the effectiveness of extremely low frequency data in discriminating the targets. The following are some suggestions for future research. An entire target response is used for statistical

analysis in Chapter 5. The work can be extended to extract target features like quadrature peak frequency, peak width, low frequency asymptote, and 3dB frequency that might serve to efficiently discriminate among the targets. Besides, the data used in discrimination are from vertically oriented (axially excited) objects whereas in reality, the buried UXO are arbitrarily oriented. Therefore, ELF data for different orientations of the target should be studied to extract orientation dependent and independent parameters. The extracted parameters can be analyzed statistically to present a quantitative measure of discrimination improvement provided by adding ELF data. A similar analysis in time-domain by extracting features like power-law to exponential transition time and decay rate should also be investigated.

Bibliography

[1] Article on unexploded ordnance in Wikipedia, an online encyclopedia, Available online at http://en.wikipedia.org/wiki/UXO

[2] About UXO thrust area on SERDP, Available online at http://www.serdp.org/general/about/thrusts/uxo.pdf

[3] D. Butler, E. Cespedes, K. O'Neill, S. Arcone, J. Llopis, J. Curtis, J.Cullinane, and C. Meyer, "Overview of Science and Technology Program For JPG Phase IV," in *Proceedings of UXO/Countermine Forum*, 1998.

[4] Information on UXO detection, Available online at http://www.uxoinfo.com/uxoinfo/detection.cfm

[5] Unexploded Ordnance (UXO): An Overview - Oct.1996, Available online at http://www.denix.osd.mil/denix/Public/Library/Explosives/uxo/uxo.html

[6] D. K. Butler, D. E. Yule, and H. H. Bennett, "Employing Multiple Geophysical Systems to Enhance Buried UXO "Target Recognition" Capability," Proceedings of the 24th US Army Science Conference, Orlando, FL, Nov 28 - Dec 2, 2004.

[7] "Assessment of detection technologies," *Metal Detectors and PPE Catalogue 2005*, Geneva International Centre for Humanitarian Demining, pp. 153 - 160 Available online at http://www.gichd.ch/fileadmin/pdf/publications/Metal_Detectors_2005/Detector_Catalogue_2005_Annex1.pdf

[8] "Detecting Unexploded Ordnance (UXO)," Available online at http://www.cflhd.gov/agm/engApplications/SubsurfaceChartacter/634Detect UnexplodedOrdnance.htm

[9] D. Butler, "Report on a workshop on electromagnetic induction methods for UXO detection and discrimination,", The Leading Edge, vol. 23, no. 8, Aug 2004, pp. 766-770. Available online at http://el.erdc.usace.army.mil/uxo/pdfs/tle04-butler.pdf

[10] I.J. Won and H. Huang, "Magnetometers and electro-magnetometers," The Leading Edge, vol. 23, no. 5, May 2004, pp. 448-451. Available online at http://www.geophex.com/Publications/mag%20emag.pdf

[11] J. R. McDonald, H. H. Nelson, J. Neece, Richard Robertson, and R. A. Jeffries, "MTADS Unexploded Ordnance Operations at the Badlands Bombing Range, Pine Ridge Reservation, Cuny Table, SD, Jul. 1997," NRL/PU/6110–98-353.

[12] Abstract on SERDP project UX-1315, Available at http://www.serdp.org/research/UX/UX-1315.pdf

[13] C. E. Baum, "Low frequency near-field magnetic scattering from highly conducting, but not perfectly conducting bodies," Interaction Note 499, Phillips Laboratory, Nov 1993.

[14] C. E. Baum, *Detection and Identification of Visually Obscured Targets*, Taylor and Francis, 1999 (Chapter 6).

[15] Kaczkowski, P.J., and D. Gill, "Pulsed Electromagnetic Induction as a UXO Detection Technology," *in Proceedings of UXO/Countermine Forum*, Williamsburg, Virginia, Mar. 1996.

[16] B. Barrow, N. Khadr, and H. H. Nelson, "Performance of Electromagnetic Induction Sensors for Detecting and Characterizing UXO," *Proceedings of the UXO Forum*, 1996, pp. 308-314.

[17] L. R. Pasion, and D. W. Oldenburg, "Locating and Characterizing Unexploded Ordnance Using Time Domain Electromagnetic Induction," Technical Report ERDC/GSL TR-01-10, U.S. Army Corps of Engineers, Engineer Research and Development Center, Vicksburg, MS, 2001.

[18] L. R. Pasion, "Discrimination of UXO Using Time Domain Electromagnetic Induction," in *Proceedings of UXO/Countermine Forum*, New Orleans, 9-12 Apr. 2001.

[19] L. R. Pasion, and Oldenburg, D.W., "A Discrimination Algorithm for UXO Using Time Domain Electromagnetics," *Journal of Engineering and Environmental Geophysics*, 28, no. 2, pp. 91-102., 2001.

[20] E. Gasperikova, "A newgeneration EM system for the detection and classification of buried metallic objects," Technical Report, Lawrence Berkely national Laboratory, University of California, Berkeley, CA, Mar. 2005.

[21] F. Morrison, T. Smith, A. Becker, E. Gasperikova, " Detection and Classification of Buried Metallic Objects UX-1225," Technical Report, Lawrence Berkely national Laboratory, University of California, Berkeley, CA, Mar. 2005.

[22] S. V. Chilaka, D. L. Faircloth, L. S. Riggs, M. E. Baginski, "A Comparison of Discrimination Capabilities of Time- and Frequency-Domain Electromagnetic Induction Systems" *Proceedings of 2005 SPIE Conference*, vol. 5794, Orlando, FL, Mar 28-Apr 1, 2005.

[23] T. H. Bell, B. J. Barrow, and J. T. Miller, "Subsurface discrimination using electromagnetic sensors," *IEEE Transactions on Geoscience and Remote Sensing*, vol. 39, pp. 1286-1293, Jun. 2001.

[24] I. J. Won, D. A. Keiswetter, and E. Novikova, "Electromagnetic Induction Spectroscopy," *Journal of Environmental Engineering Geophysics*, vol. 3, no. 1, pp. 27-40, 1998.

[25] D. A. Keiswetter, I. J. Won, J. Miller, T. Bell, E. Cespedes, K. O'Neill, "Discriminating capabilities of multifrequency EMI data," in *Proceedings of IEEE International Geoscience and Remote Sensing Symposium*, vol. 4, Honolulu, HI, 24-28 Jul. 2000, pp. 1415-1417.

[26] H. Huang, I. J. Won, "Characterization of UXO-like targets using broadband electromagnetic induction sensors," *IEEE Transactions on Geoscience and Remote Sensing*, vol. 41, no. 3, pp. 652-663, Mar. 2003.

[27] H. H. Nelson, B. Barrow, T. Bell, R. S. Jones, B. SanFilipo, "Frequency-Domain Electromagnetic Induction Sensors for the Multi-Sensor Towed Array Detection System," NRL/MR/6110–02-8650, Nov. 2002.

[28] K. O'Neill, S. Haider, F. Shubitidze, K. Sun, C. O. Ao, H. Braunisch, and J. A. Kong, "Ultra-wideband electromagnetic induction spectroscopy," in *Proceedings of UXO/Countermine Forum*, New Orleans, 9-12 Apr. 2001. Available: http://ceta.mit.edu/chi/uxo01_induction.pdf

[29] P. Gao, L. Collins, N. Geng, L. Carin, "Classification of buried metal objects using wideband frequency-domain electromagnetic induction responses: a comparison of optimal and sub-optimal processors" in *Proceedings of IEEE International Geoscience and Remote Sensing Symposium*, vol. 3, 28 Jun-2 Jul 1999, pp. 1819 - 1822.

[30] A. B. Tarokh, E. L. Miller, I. J. Won and H. Huang, Statistical classification of buried objects from spatially sampled time or frequency domain electromagnetic induction data, Radio Science, vol 39, no. 4, Jun, 2004, RS4S05-1-RS4S05-11

[31] S. V. Chilaka, L. S. Riggs, H. H. Nelson, T. H. Bell, "Extremely Low Frequency Response (Below 30 Hz) of UXO-Like Objects" in *Proceedings of 2004 SPIE Conference*, vol. 5415, Orlando, FL, 12-16 April, 2004.

[32] S. V. Chilaka, D. L. Faircloth, L. S. Riggs, H. H. Nelson, "Enhanced Discrimination among UXO-like Targets Using Extremely Low Frequency Magnetic Fields" Submitted to *IEEE Transactions on Geosciences and Remote Sensing*, Dec. 2004.

[33] Article on Polish mine detector in Wikipedia, an online encyclopedia, Available online at http://en.wikipedia.org/wiki/PolishMineDetector

[34] J. R. Wait, "A conducting sphere in a time-varying magnetic field," *Geophysics*, vol. 16, pp. 666-672, 1951.

[35] F. S. Grant, and G. F. West, *Interpretation Theory in Applied Geophysics*, New York: McGraw-Hill, 1965 (Chapter 17).

[36] R. F. Harrington, F. S. Grant, and G. F. West, *Time-Harmonic Electromagnetic Fields*, New York: McGraw-Hill, 1961.

[37] Y. Zhang; L. Collins, H. Yu; C.E. Baum, L. Carin, "Sensing of unexploded ordnance with magnetometer and induction data: theory and signal processing," *IEEE Transactions on Geoscience and Remote Sensing*, vol. 41, no. 5, pp. 1005-1015, May 2003.

[38] J. T. Miller, T. H. Bell, J. Soukup, D. Keiswetter, "Simple Phenomenological Models for Wideband Frequency-Domain Electromagnetic Induction," *IEEE Transactions on Geoscience and Remote Sensing*, vol. 39, no. 6, pp 1294-1298, Jun. 2001.

[39] I. Shamatava, K. O'Neill, F. Shubitidze, K. Sun, C. O. Ao, "Evaluation of approximate analytical solutions for EMI scattering from finite objects of different shapes and properties," in *Proceedings of IEEE International Geoscience and Remote Sensing Symposium*, vol. 3, Toronto, Canada, 24-28 Jun. 2002, pp. 1550-1552a.

[40] F. Shubitidze, K. O'Neill, K. Sun, K. D. Paulsen, "Investigation of broadband electromagnetic induction scattering by highly conductive, permeable, arbitrarily shaped 3-D objects," *IEEE Transactions on Geoscience and Remote Sensing*, vol. 42, no. 3,pp. 540-556, Mar. 2004.

[41] C. O. Ao, H. Braunisch, K. O'Neill, J.A. Kong, "Quasi-magnetostatic solution for a conducting and permeable spheroid with arbitrary excitation," *IEEE Transactions on Geoscience and Remote Sensing*, vol. 40, no. 4, pp. 887-897, Apr. 2002.

[42] H. Braunisch, C. O. Ao, K. O'Neill, J.A. Kong, "Magnetoquasistatic response of conducting and permeable prolate spheroid under axial excitation," *IEEE Transactions on Geoscience and Remote Sensing*, vol. 39, no. 12, pp. 2689-2701, Dec. 2001.

[43] B. E. Barrowes, K. O'Neill, T. M. Grzegorczyk, X. Chen, J. A. Kong, "Broadband Analytical Magnetoquasistatic Electromagnetic Induction Solution for a Conducting and Permeable Spheroid," *IEEE Transactions on Geoscience and Remote Sensing*, vol. 42, no. 11,pp. 2479 - 2489, Nov. 2004.

[44] K. O'Neill, K. Sun, F. Shubitidze, I. Shamatava, J. Curtis, J. Simms, " UXO Discrimination: Near Field, Heterogeneous and Multiple Objects," UXO/Countermine Forum, Sept.3-6, 2002, Orlando, FL.

[45] X. Liao and L. Carin, "Application of the Theory of Optimal Experiments to Adaptive Electromagnetic-Induction Sensing of Buried Targets," *IEEE Transactions on Pattern Analysis and Machine Intelligence*, vol. 26, no. 8, pp. 961-972, Aug. 2004.

[46] F. Shubitidze, K. O'Neill, S. Haider, K. Sun, K. D. Paulsen, "Application of the method of auxiliary sources to the wide-band electromagnetic induction problem," *IEEE Transactions on Geoscience and Remote Sensing*, vol. 40, no. 4, pp. 928-942, Apr. 2002.

[47] K. Sun, K. O'Neill, F. Shubitidze, S. Haider, K. D. Paulsen, "Simulation of electromagnetic induction scattering from targets with negligible to moderate penetration by primary fields," *IEEE Transactions on Geoscience and Remote Sensing*, vol. 40, no. 4, pp. 910-927, Apr. 2002.

[48] F. Shubitidze, K. O'Neill, I. Shamatava, K. Sun, K. D. Paulsen, "Fast direct and inverse EMI algorithms for enhanced identification of buried UXO with real EMI data" in *Proceedings of IEEE International Geoscience and Remote Sensing Symposium*, vol. 7, 21-25 Jul. 2003, pp. 4160-4162.

[49] K. Sun, K. O'Neill, F. Shubitidze, I. Shamatava, K. D. Paulsen, "Application of TSA formulation for inversion of a metallic object's electromagnetic properties from EMI data," in *Proceedings of IEEE International Geoscience and Remote Sensing Symposium*, vol. 6, 21-25 Jul. 2003, pp 3860-3862.

[50] F. Shubitidze, K. O'Neill, S. Haider, K. Sun, K. D. Paulsen, "Analysis of induction responses from metal objects using the method of auxiliary sources," in *Proceedings of International Conference on Mathematical Methods in Electromagnetic Theory*, vol. 2, 12-15 Sep. 2000, pp. 468-470.

[51] F. Shubitidze, K. O'Neill, I. Shamatava, K. Sun, K. D. Paulsen, "Implementation a hybrid MAS and SPA algorithm for broadband electromagnetic induction problems," in *Proceedings of the 7th International Seminar/Workshop on Direct and Inverse Problems of Electromagnetic and Acoustic Wave Theory*, 10-13 Oct. 2002, pp. 33-37.

[52] F. Shubitidze, K. O'Neill, K. D. Paulsen, "The method of auxiliary sources for analysis low frequency EM field scattering from composite object," Shubitidze, F.; O'Neill, K.; Paulsen, K.D.; in *Proceeding of IEEE Antennas and Propagation Society International Symposium*, vol. 2, 8-13 Jul. 2001, pp. 522-525.

[53] N. Geng, A. Sullivan, L. Carin, "Multilevel fast-multipole algorithm for scattering from conducting targets above or embedded in a lossy half space," *IEEE Transactions on Geoscience and Remote Sensing*, vol. 38, no. 4, pp. 1551-1560, Jul. 2000.

[54] L. Carin, H. Yu; Y. Dalichaouch, A. R. Perry, P. V. Czipott, C. E. Baum, "On the wideband EMI response of a rotationally symmetric permeable and conducting target," *IEEE Transactions on Geoscience and Remote Sensing*, vol. 39, no. 6, pp. 1206-1213, Jun. 2001.

[55] N. Geng, P. Garber, L. Collins, L. Carin, D. Hansen, D. Keiswetter, I. J. Won, "Wideband Electromagnetic Induction for Metal-Target Identification: Theory, Measurement and Signal Processing," Technical Report, Duke University, Durham, NC, Sep. 1997.

[56] N. Geng, C. E. Baum, L. Carin, "On the low-frequency natural response of conducting and permeable targets," *IEEE Transactions on Geoscience and Remote Sensing*, vol. 37, no. 1, pp. 347-359, Jan. 1999.

[57] D. L. Faircloth, S. V. Chilaka, L. S. Riggs, M. E. Baginski, "A Finite Element Method for the Electromagnetic Characterization of Quasi-Magnetostatic Problems Found in UXO Detection and Discrimination," *Proceedings of 2004 Applied Computational Electromagnetics Society Conference*, Syracuse, NY, Apr 19-23, 2004.

[58] I. J. Won, D. A. Keiswetter, D. R. Hanson, E. Novikova, T. M. Hall, "GEM-3: A Monostatic broadband electromagnetic induction sensor," *Journal of Engineering and Environmental Geophysics*, vol. 2, no. 1, pp. 53-64., Mar 1997.

[59] P. P. Silvester, D. Omeragic, "Sensitivity maps for metal detector design," *IEEE Transactions on Geoscience and Remote Sensing*, vol. 34, no. 3,pp. 788-792, May 1996.

[60] P. Kašpar, P. Ripka, "Induction Coils: voltage versus current output," *Imeko World Congress*, Vienna, vol. 5, pp. 55-60, 2000.

[61] R.J. Prance, T.D. Clark, H. Prance, "Compact broadband gradiometric induction magnetometer system," Sensors and Actuators, vol 76, pp. 117-121, 1999.

[62] J. N. Palasagaram, *Efforts towards the designa and development of an electromagnetic induction sensor optimized for detection and discrimination of unexploded ordnance*, Master's Thesis, Auburn University, 2006.

[63] Wikipedia contributors, "Lyapunov's central limit theorem — Wikipedia, The Free Encyclopedia," http://en.wikipedia.org/w/index.php?title=Lyapunov's_central_limit_theorem&oldid=37679120, Online; Accessed on: 9 Feb 2006.

[64] H. Stark and J. W. Woods, *Probability and Random Processes with Applications to Signal Processing*, 3rd ed, Prentice Hall, 2001.

[65] M.D. Srinath, P.K. Rajasekaran, R. Viswanathan, *Introduction to Statistical Signal Processing with Applications*, New Jersey: Prentice-Hall, Inc, 1995.

[66] H. V. Poor, *An Introduction to Signal Detection and Estimation*, 2nd Edition, Springer-Verlag, 1994.